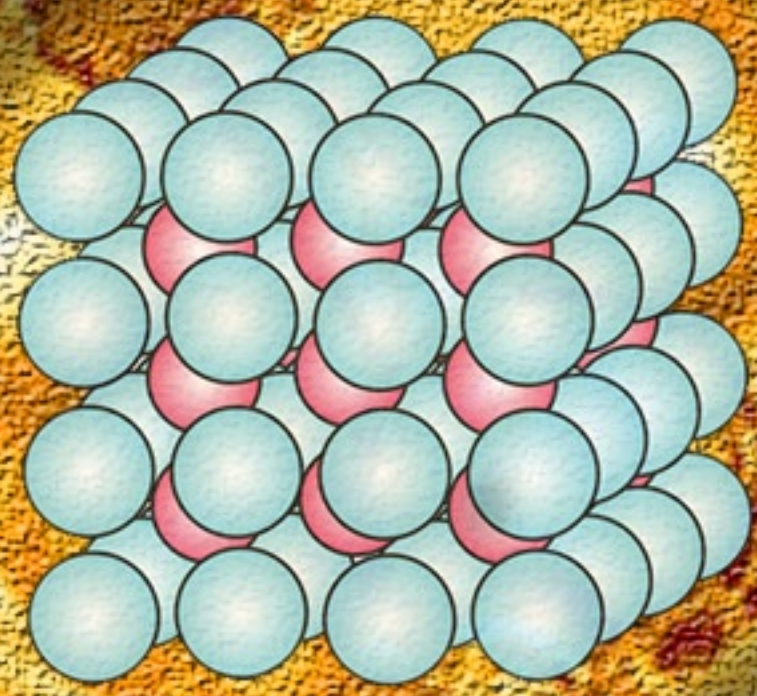
INTERNATIONAL SCIENTIFIC JOURNAL

"MATERIAL SCIENCE"



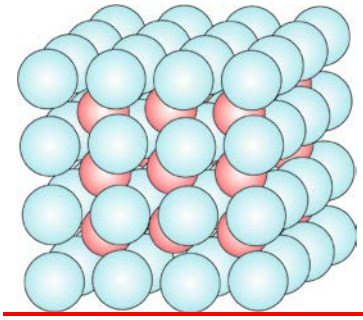
„NONEQUILIBRIUM PHASE TRANSFORMATIONS"

YEAR IX, ISSUE 2/2023

ISSN PRINT 2367-749X
ISSN WEB 2534-8477

PUBLISHER: SCIENTICIC TECHNICAL UNION OF MECHANICAL ENGINEERING INDUSTRY 4.0

108 Rakovski str., 1000 Sofia, Bulgaria
tel./fax (+359 2) 986 22 40, tel. (+359 2) 987 72 90,
office@stumejournals.com, www.stumejournals.com



INTERNATIONAL SCIENTIFIC JOURNAL

MATERIALS SCIENCE. NON-EQUILIBRIUM PHASE TRANSFORMATIONS

PUBLISHER:

SCIENTIFIC TECHNICAL UNION OF MECHANICAL ENGINEERING "INDUSTRY 4.0"

108, Rakovski Str., 1000 Sofia, Bulgaria
tel. (+359 2) 987 72 90,
tel./fax (+359 2) 986 22 40,
office@stumejournals.com

ISSN PRINT 2367-749X, ISSN WEB 2534-8477
YEAR IX, ISSUE 2/2023

EDITORIAL BOARD

CHIEF EDITOR

Prof. Tsanka Dikova, BG

DEPUTY EDITOR:

Dr. Alexander Krugljakow, Germany
Prof. Sergey Dobatkin, Russia
Prof. Sergey Nikulin, Russia
Prof. Victor Anchev, Bulgaria

MEMBERS:

Prof. Adel Mahmud, Iraq
Prof. Anna Proikova, Bulgaria
Prof. Bekir Sami Yilbas, Saudi Arabia
Prof. Dermot Brabazon, Ireland
Prof. Dipten Misra, India
Assoc. Prof.Eugeniy Grigoriev, Russia
Prof. F. W. Travis, United Kingdom
Prof. Gennagiy Bagluk, Ukraine
Assoc. Prof. Ibrahim E.Saklakoglu, Turkey
Prof. Iis Sopyan, Malaysia
Prof. Ivan Parshorov, Bulgaria
Prof. Ivanja Markova, Bulgaria
Prof. Janez Grum, Slovenia
Prof. Jens Bergstrom, Sweden
Prof. Leszek Dobrzanski, Poland
Prof. Ludmila Kaputkina, Russia
Prof. Nikolai Dulgerov, Bulgaria
Prof. Omer Keles, Turkey
Prof. Plamen Danev, Bulgaria
Prof. Rui Vilar, Portugal
Prof. Rusko Shishkov, Bulgaria
Prof. Saleem Hashmi, Ireland
Dr. Sefika Kasman, Turkey
Prof. Seiji Katayama, Japan
Prof. Souren Mitra, India
Dr. Sumsun Naher, United Kingdom
Prof. Svetlana Gubenko, Ukraine
Prof. Sveto Cvetkovski, Macedonia
Prof. Ventsislav Toshkov, Bulgaria
Prof. Yovka Dragieva, Bulgaria

C O N T E N T S

Physical vapor deposited coatings with shape memory effect
Slavcho Topalski, Teja Roch, Axel Zwick, Christoph Leyens 35

The influence of the copper amount on structure and properties formation of aluminum-matrix composite materials
Yevheniia Kyryliuk, Oksana Baranovska, Stepan Kyryliuk, Konstantin Petrash, Gennadii Bagliuk 38

Optical Logic Half Adder Based On Multi Ring Resonators Silicon Photonic Crystal Structures
Moria Gulitski, Yonatan Pugachov, Omri Mizrahi, Dror Malka 41

The possibility of optimizing the properties of materials by using carbon nanostructures
Halina Yu. Mykhailova 48

Al-Si-Ni composite with a low-temperature coefficient of linear expansion
Inna Kirian, Alexander Rud, Tetiana Monastyrska, Gennadiy Bagliuk, Andrey Lakhnik, Viktor Nosenko, Mykola Skoryk, Vitalii Bevz, Dmytro Pakula 51

Long-time phase transitions in various vegetable oils
Leszek T. Pawlicki 54

Mechanical and microstructure features of ti-al damping materials
Denys V. Oryshych, Oleksandr O. Stasiuk, Dmytro V. Pakula, Vasyl I. Nevmerzhytskyi, Vasyl P. Tkachuk 56

Effects of magnetohydrodynamic treatment and alloying on the structure and properties of Al-Si-Mg casting alloys
Tetiana Monastyrska, Alla Berezina, Oleh Molebny, Vladyslav Fikssen 59

Study of fatigue failure for carburized carbon steel
Nardeen Al-Saiymari 62

Physical vapor deposited coatings with shape memory effect

Slavcho Topalski[1], Teja Roch[1], Axel Zwick[1], Christoph Leyens[1,2]
[1]Fraunhofer IWS; Eberhardstr. 12; 44141 Dortmund; Germany
[2]Institute of Materials Science; TUD Dresden University of Technology; Helmholtzstraße 7; 01069 Dresden; Germany
E-mail: slavcho.topalski@iws.fraunhofer.de

Abstract: *Shape memory effects have been observed not only in bulk materials but also in PVD thin films. We have deposited copper-base shape memory alloys (SMAs) on Al substrates using DC sputtering. The coatings exhibit diffusionless transformation from the high-temperature austenite phase to the low-temperature martensite phase. This can be both, thermally controlled as a kind of two-way memory effect and stress-induced, giving a pseudoelastic behavior. The structures and microstructures of the coatings were analyzed by X-ray diffraction and optical microscopy. The martensitic transformation temperature was determined by dilatometric measurement. The coatings exhibit a martensite start temperature (Ms) very close to that of bulk materials. The SMA thin films have the ability to recover from large transformation stresses and strains when heated. In addition, their pseudoelasticity makes them potentially suitable as a protective layer against cavitation erosion.*

Keywords*: PHASE TRANSFORMATIONS, SHAPE MEMORY, PVD COATINGS.*

1. Introduction

The SME (shape memory effects), one-way memory effect, thermoelasticity and pseudoelasticity are closely related to each other and are all based on a martensitic transformation [1]. The SME have been observed not only in bulk materials, but also in PVD (Physical Vapor Deposition) thin films. Along with the superior SME properties, the high strength in combination with cavitation erosion resistance [2, 3] as well as their anti-corrosion properties [4] are interesting for further research. Based on the constituent elements, these materials can be classified into TiNi-, Cu-, and Fe-based alloys. An example for a copper-based shape memory alloy are alloys with Cu and Al. However, for these alloys, with increasing Al concentration, the formation of the brittle γ2-phase can occur, even after rapid cooling. This typically inhibits thermoelastic martensitic transformation. The addition of Ni can stabilize the high-temperature β1-phase. Here, diffusion between Cu and Al is hindered and the β1-β1'-deformation transformation is facilitated (see Ref. [5]). Since the onset of martensitic transformation Ms of the alloys with Al content of 14 wt% and Ni in the range of 4 to 4.5 wt% is just below 0°C [2], these alloys found wide practical application as a material for structural elements with superelastic shape memory effect. The workability of components made of Cu-Al-Ni-based alloys, can be additionally improved by the introduction of Ti and Mn. The addition of Ti refines the grains, which, for example, facilitates plastic deformation when heat is applied.

Due to the different vapor pressures of the individual components, it can be extremely difficult to control the chemical composition of alloy coatings. Potential vacuum processes for the production of alloys are shown in Fig. 1. Plasma spraying of alloyed powder in vacuum can be effective for coatings with a thickness of more than 100 µm. At a constant temperature, a uniform coating can be achieved with a thermal evaporator if the amount of material in the crucible is constant. In this case, material must be continuously fed into the crucible and evaporated.

Flash evaporation provides exceptionally high accuracy of chemical composition both in the thickness of the coating and on the surface of the substrate. This is due to the fact that the granules are evaporated, as soon as they are fed to the heated crucible. Additionally the composition of the vapor corresponds to the original alloy material. [7]. With magnetron sputtering and in pulsed operation, it is basically possible to transfer the alloy compositions of the target material to the deposited layer. Differences of the order of 0.5 at. % come from the differences in sputtering ratio, irregular target wear, and difficulty in sputtering of ferromagnetic metals (Ni). This has established magnetron sputtering as the primary method for producing SME alloy coatings. In cathodic arc evaporation, local melting occurs from an electric arc discharge moving along the surface of the target. The metal vapors of the arc process are almost completely ionized. This makes it possible to apply a negative potential to the substrate to obtain homogeneous coatings with high density [6]. The above advantages combined with high coating deposition rate, good adhesion and low cost power supply have established arc evaporation as the leading coating method for tools and other components. One major problem of arc evaporation compared to magnetron sputtering might be a higher roughness of the coatings. This results from locally molten regions on the targets, where the metal vapor expands and pushes the melt away from the cathode surface. As a result, metal droplets can reach the substrate and cause defects in the formation and growth of the layer leading to an increase in roughness. This disadvantage can be eliminated by using a suitable filter system. Whereby appropriate filter systems lead to a higher material consumption of the target.

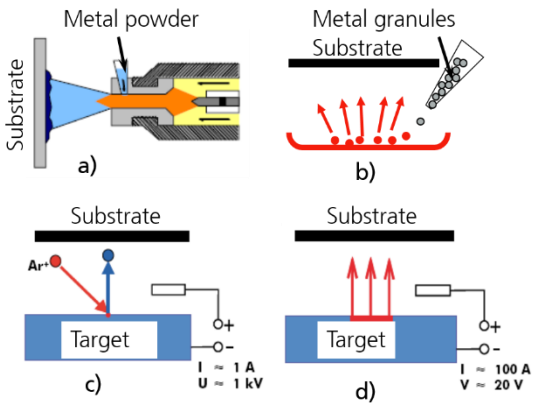


Fig. 1 *Potential methods for PVD alloy coatings: a) plasma spraying in vacuum, b) flash evaporation, c) magnetron sputtering, d), arc evaporation [6].*

2. Experiments

To fabricate the targets, the corresponding material was molten in an argon arc vacuum furnace using a water-cooled copper crucible. After alloying, the targets were diffusion annealed for 8 hours at 950 °C in an argon environment for homogenization. The starting and finishing temperatures of the martensitic and austenitic transitions were determined by dilatometric analysis of melt spinning strips from the target material. The coatings were prepared with a laboratory equipment of VEB - Hochvakuum Dresden type B55.3-1 and deposited on a water-cooled aluminum foil. During the experiments, the pressure in the vacuum was kept constant at $8x10^{-1}$ Pa and the target substrate distance was 170 mm. The substrate speed was changed from 1.67 to 5 mm/min and the discharge current magnitude from 1.5 to 3.5 A. One of the disadvantages of magnetrons with toroidal discharge can be non-uniformity of ion current density on the surface of the target and, consequently, non-uniform flow of the sputtered material. Uniformity of the thickness of the deposited layers was achieved by moving the substrate relative to the target. The substrates were moved using a roll-to-roll system (Fig. 3). The chemical composition of the alloys was determined by point WDX analysis using an X-ray microanalyzer

on a JEOL SUPERPROBE 733 scanning microscope. Furthermore, information on the crystal structure and crystal lattice parameters were obtained by XRD structure analysis (Cu-Kα) with X-ray diffractometer (Bourevestnik company, model DRON-2). The temperatures of the phase transitions were measured during cooling and heating with a band dilatometer. Color changes due to martensitic transformations were studied to determine shape memory properties. Microstructural analysis of the alloys produced in the argon arc furnace was performed using a metallographic microscope (company Carl Zeiss Jena, model Epitip 2). Information on the crystal structure and lattice parameters was obtained by TEM analysis using an EMB-100L microscope.

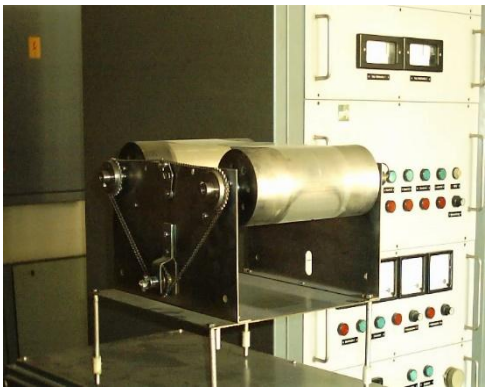


Fig. 3 *The roll-to-roll system, which was used to move the substrate.*

3. Results and discussion

The starting alloys used to make the targets had the following compositions:

- Alloy 1: Cu-12.8Al-3.3 Ni (wt. %)
- Alloy 2: Cu-14.1Al-4.2Ni (wt. %)

According to the X-ray structural analysis in Fig. 4 and the literature data [8], the selected alloys have the following phase composition at room temperature:

Alloy 1: Martensite with twinned structure γ_1' with 2H crystal lattice; Martensite β_1' with 18R crystal lattice and β_1 with DO3 superstructure.

Alloy 2: The high temperature β_1 with DO3 superstructure and the γ_2 phase.

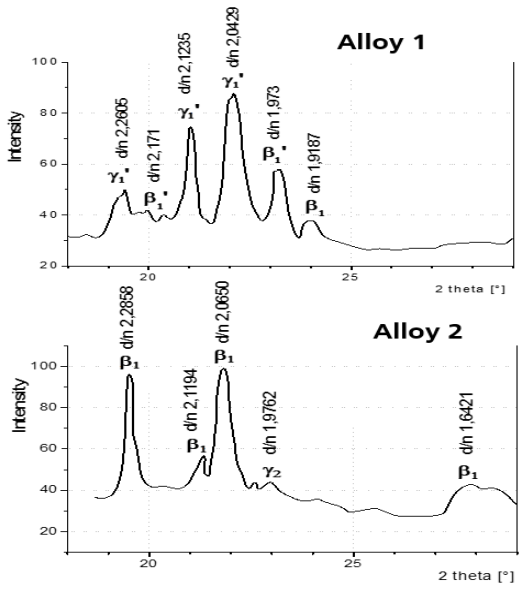


Fig. 4 *X ray diffraction of the targets after homogenization annealing at 950°C for 8h and cooling in water a) Alloy 1: Cu-12.8Al-3.3Ni wt. % b) Alloy 2:. Cu-14.1Al-4.2Ni wt. %.*

The parameters that influence the thickness and morphology of the coatings are:

- the speed at which the substrate moves
- the working pressure (vacuum)
- the target - substrate distance
- the magnitude of the discharge current

The coating thicknesses in Fig. 5 illustrate the correlations between coating thickness, discharge currents and substrate speed. Increasing the discharge current in combination with a higher substrate speed leads to both, an increase in coating thickness and a finer microstructure (not shown in this publication). It is known that, in β Cu-Al-Ni alloys with decreasing grain size, the tensile strength and fatigue limit increase, and the Ms temperature decreases [9].

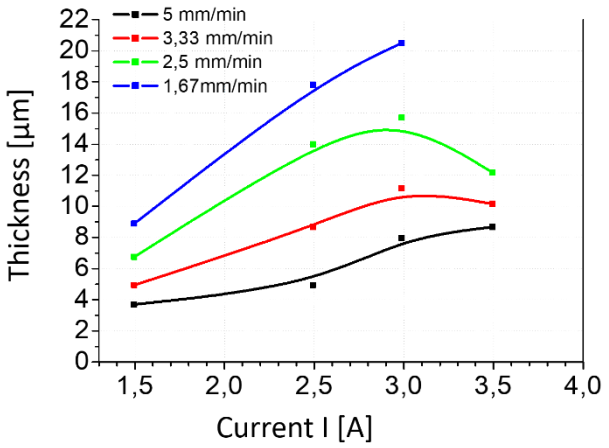


Fig. 5 *Experimental curves of coating thickness, discharge currents and substrate speed.*

When alloyed targets are used, the following can be observed: A decrease in Ni and Al content, an increase in Cu content, in the crystal matrix and a martensitic structure of the coatings (fig. 6a). Due to the different sputtering rates and angular distributions of Al and Cu, the design and composition of the sputtering targets are essential. In magnetron sputtering the deposition rate is influenced by the depth of the sputter trench and therefore changes with sputtering duration, especially when magnetic materials like elemental Ni are deposited. As a result of collisions with the sputtering gas, the atoms even lose a considerable part of their initial energy on their way to the component surface. Images of the sputtered layers with a scanning electron microscope show a columnar (porous) structure.

The microstructural analysis for alloy 1 (Fig. 6a) recorded the simultaneous presence of deformation martensite γ_1' with regular and parallel martensitic crystals and β_1' martensite with small needle-like crystals. The structure of alloy 2 (Fig. 6b) is made up of large light grains of phase β_1 (Cu3Al) and numerous small needle-like crystals of deformation martensite β_1'. After homogenization annealing for 2 hours at 950°C and cooling in water, according to the XRD analysis (Fig. 4b), the targets are composed of the β_1 phase with DO3 (L21) ordered austenite crystal structure at room temperature.

The characteristic phases of strip samples with selected chemical composition were studied with a TEM. The microstructures and corresponding electron patterns are presented in Fig. 7. The structure of the alloy 2 (Cu14.1Al4.2Ni) is composed of large light grains according to the electronograms of the β_1 (Cu3Al) phase and numerous small dark grains of the γ_2 (Cu9Al4) and γ_1 (Cu3Al2) phases. However the analysis of alloy 1 (Cu12.8Al3.3Ni) recorded the simultaneous presence of deformation martensite γ_1' with regular and parallel martensite crystals and β_1' martensite with small needle-like crystals. Some of the reflexes correspond to the β_1 and γ_2 phases. The resulting coatings do not differ in phase composition from the sputter targets.

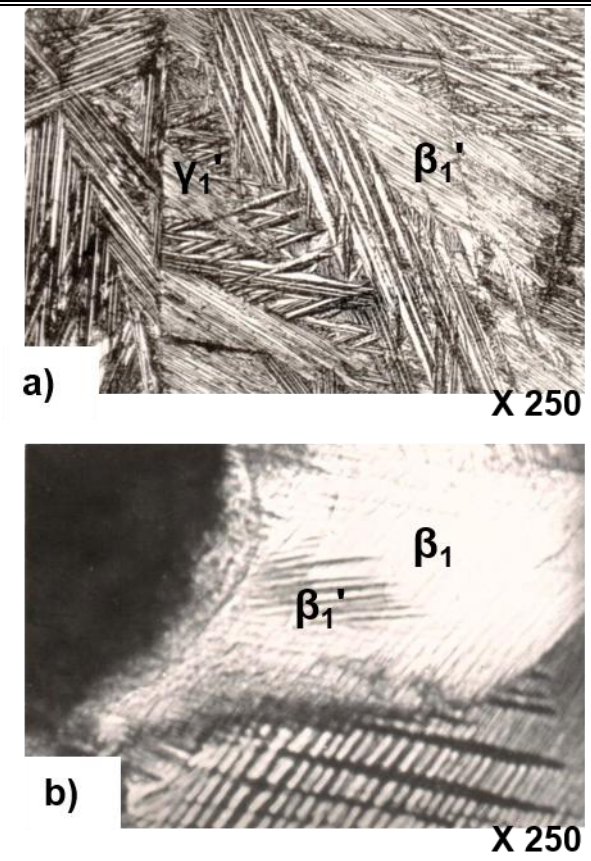


Fig. 6 *Microstructure of Cu-Al-Ni alloys of targets: a) martensitic Cu12.8Al3.3Ni b) pseudoelastic Cu14.1 Al4.2Ni.*

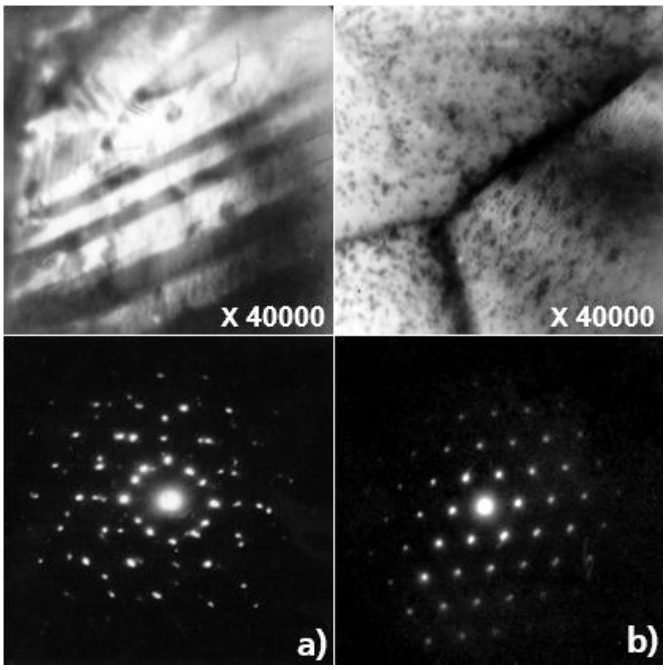


Fig. 7 *TEM microstructures and electronograms of Cu-Al-Ni alloy coatings: a) martensitic Cu12.8Al3.3Ni b) pseudoelastic Cu14.1 Al4.2 Ni*

According to [10], alloys are copper-coloured when they are made of high-temperature β_1, and golden-coloured when γ_1' martensitic is present. When alloy coatings are heated above 150°C, their colour changes from golden yellow to copper red. This shows that the martensitic-austenite transformation takes place at around 150°C. The change in the optical properties of the coatings is observed during deformation. In the case of bending, the coating of alloy 2 changes from copper red to golden yellow and vice versa, when the deformation is removed, the colour is restored. The structural transformation is not caused by a change in temperature but by the effect of mechanical stress. Due to the external load, the martensitic structure also occurs above the Ms temperature, which makes the work piece deformable. When the force is removed, the austenite phase returns and the original form emerges.

4. Conclusion

Within our work, shape memory alloys could be successfully deposited as thin films. We found:

1. SME alloy coatings produced by magnetron sputtering are comparable in properties to those produced by casting, spin coating or powder metallurgy.
2. An increase in magnetron discharge current combined with a higher substrate speed results in both, an increase in coating thickness and a finer microstructure. The fine grain structure of the coatings gives them an advantage over conventional alloys.
3. The phase transformation from a martensitic to an austenitic structure made it possible to change the color of the surfaces.

In conclusion the fact that the coating parameters can be used to refine the microstructure, which increases the fatigue limit, improves the possibility of industrial application. Furthermore, it is conceivable to measure stresses in components with appropriate coatings.

Acknowledgements

The experimental investigations and the preparation of the samples in this publication were carried out at the University of Ruse in Bulgaria. Dr. S. Topalski was assisted by Dr. P. Etarska in the preparation of the measurement results. For the preparation of the coatings we would like to thank Dr. V. Etarski.

References

1. R. V. Krishnan, L. Delaey, H. Tast, H. Warlimont, „Thermoplasticity, pseudoelasticity and the memory effects associated with martensitic transformations“, Journal of Materials Science 9 (1974) 1536-1544
2. R.H. Richman, A.S. Rao, D. Kung, “Cavitation erosion of NiTi explosively welded to steel”, Daedalus Associates, Inc., Mountain Kew, CA 94043, USA b Powertech Labs Inc., Surrey, BC V3W 7R7, Canada Wear 181-183 (1995) 80-85
3. L.M. Yang, A.K. Tieu, D.P. Dunne, S.W. Huang, H.J. Li, D.Wexler, Z.Y. Jiang, “Cavitation erosion resistance of NiTi thin films produced by Filtered Arc Deposition”, Wear 267 (2009) 233–243
4. Gianni Rondelli, “Corrosion resistance tests on NiTi shape memory alloy”, Biomaterials 17 No 20 (1996), Elsevier Science Limited
5. K. Otsuka, H. Sakamoto, K. Shimizu, „Successive stress-induced martensitic transformations and associated transformation pseudoelasticity in Cu-Al-Ni alloys“, Metallurgical Volume 27, Issue 4, April (1979), Pages 585-601
6. B. Schultrich, „Lexikon der Dünnschichttechnologie 2010“ Sonderausgabe der Zeitschrift. Vakuum in Forschung und Praxis (2010) WILEY-VCH Verlag GmbH & Co. KGaA, Weinheim
7. E. Makino, M. Uenoyama, T. Shibata, “Flash evaporation of TiNi shape memory thin film for microactuators”, ELSEVIER Sensors and Actuators A 71 (1998) 187-192
8. H. Warlimont, L. Delaey, „Martensitic transformations in copper-, silver-, and gold-based alloys” Pergamon Press (1974)
9. K. Mukunthan, L.C. Brawn, „Preparation and Properties of Fine Grain β CuAlNi Strain- mamory Alloys“, Metallurgical Transactions, Vol. 19a, December (1988)-2921
10. Minemura, H. Andoh, M. Nagai, R. Watanabe, S. Shimizu, I. Ikuta. „Reversible colour change in sputter-deposited Cu-AI-Ni film“.Journal of Materials Science Letters 6 (1987) 1267-1269

The influence of the copper amount on structure and properties formation of aluminum-matrix composite materials

Yevheniia Kyryliuk, Oksana Baranovska, Stepan Kyryliuk, Konstantin Petrash, Gennadii Bagliuk
Frantsevich Institute for Problems in Materials Science of the NASU, Kyiv, Ukraine, 03142

Abstract: *The phase and structure formation of aluminum-matrix composite materials reinforced with titanium carbide during their synthesis and consolidation using the forging were investigated. The influence of copper additives on the structure formation, density, porosity, and hardness of aluminum-matrix composites was determined. The research results revealed the presence of Al+Cu+TiC phases in copper-alloyed samples. Studies of density and porosity showed that the samples without copper additives were maximally densified after hot stamping and had minimal porosity, unlike the copper-alloyed composites.*
KEYWORDS: : THERMAL SYNTHESIS, MASTER ALLOY, METAL MATRIX COMPOSITE, ALUMINUM, STRUCTURE, PHASE COMPOSITION, TITANIUM CARBIDE

1. Introduction

Thanks to their high specific modulus (E/ρ) and yield stress (σe/ρ), Metal Matrix Composites (MMCs) have attracted attention from researchers and industry as being unique materials for high-tech applications such as in the aerospace and automotive sectors. Compared with those of lightweight alloys (Aluminium, Magnesium and Titanium alloys), the mechanical properties of MMCs, such as strength and stiffness, are improved by the use of ceramic reinforcement. Among the commonly used reinforcements (carbon(C), boron nitride (BN), silicon carbide (SiC), titanium carbide (TiC), aluminium oxide (Al_2O_3)), TiC has been recognized as one of the most important for metal matrix composite materials due to its excellent properties (such as high hardness and high temperature stability for example). Moreover, it has been demonstrated that if the removal of the native oxide layer of TiC is ensured, good wetting and thus good adhesion can occur at the interface with metals [1,2] because a significant part of the cohesion of this carbide is assured by metallic bonds [3].

There are two different routes for achieving an Al-TiC metal matrix composite, which have been intensively explored in the literature. The first is the liquid route, that consists in mixing TiC or Ti+C powder with an Al melt using different technological processes such as stir casting or flux-assisted casting [4-15]. The second is the powder metallurgy route, starting either from a mixture of elemental Al+Ti+C powders [16,18], a mixture of Al+TiC [19] or a mixture of intermetallic compounds such as titanium trialuminide (Al_3Ti) and aluminium carbide (Al_4C_3) [17,18]. In this last case, when the starting materials are different from Al and TiC, the synthesis route is called “reactive synthesis” because Al and TiC are formed in situ from selected precursors.

As a consequence, the development of particulate-reinforced Al matrix composites with high mechanical strength and without any detrimental degradation of the damage tolerance properties (toughness, elongation) is still a key point to improve their properties and extend the number of their possible applications.

To improve mechanical properties, alumino-matric alloys are additionally alloyed with copper. The tensile strength of aluminum alloys rises with higher copper content. The strength of alloys increases with a copper content of 8%, further increasing the copper content to 10% results in a slight reduction in the strength of the alloys. The tensile strength sharply decreases when the copper content is up to 6% and shows little change with further increase up to 10%.

In this study, the influence of copper alloying in aluminum matrix composites with various compositions on the structure and mechanical properties of the alloys was investigated.

2. Objects and research methods

The initial components for the preparation of the mixtures for further thermal synthesis included powders of aluminum (PA-4), titanium (PTH-80), copper, and carbon. Three compositions of the initial mixture with the different aluminum contents (from 20 to 50 wt. %) were selected to evaluate the influence of the component ratios on the structure of the synthesized alloys. Also, the selected compositions were additionally alloyed with 5 (%, by mass) copper, in the initial charge.

Table 1. *Component content in the initial mixtures of Al-Ti-C composites*

№ of the mixture	Element content, wt %			
	Al	C	Ti	Cu
1	20	16	64	-
2	45	11	44	-
3	50	10	40	-
4	20	14,8	60,2	5
5	45	10	40	5
6	50	9	36	5

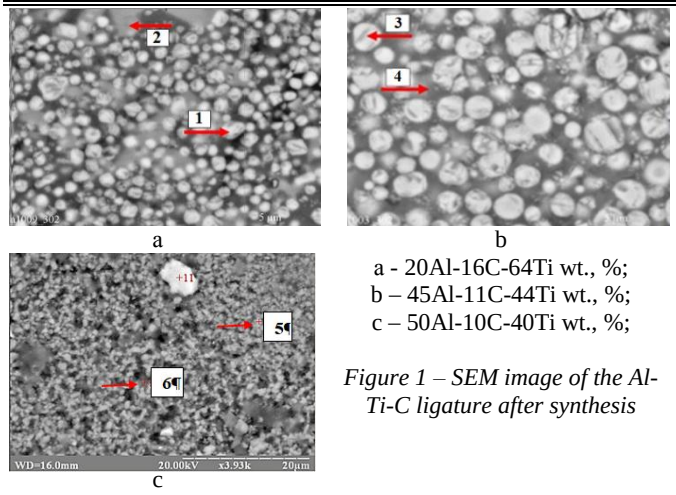
The initial mixtures were pressed under a pressure of 200 MPa, and thermal synthesis was conducted in a vacuum induction furnace at a temperature of 950°C with a holding time of 1 hour and a sintering rate of 5-10 °C/min. After thermal synthesis, the obtained blanks were heated in a laboratory electric furnace to a temperature of 520°C for 20 minutes. Prior to this, a protective mixture of silicate glue and graphite was applied to the blanks. Subsequently, the blanks were subjected to forging in a semi-closed die on a hydraulic press PG-60.

The microstructure of the synthesized composites was investigated using a scanning electron microscope with an energy-dispersive microanalyzer REM 106I, allowing for high-resolution imaging of the structure in backscattered (BSE) and secondary (SE) electrons, as well as providing information about the chemical composition and structure. Sample etching was performed in a 40% NaOH solution. X-ray phase analysis was carried out using a DRON-3M. Hardness measurements were performed using a Novotest TC-BRV instrument based on the Rockwell method (HRB scale).

3. Results and discussion

The composition of powder mixtures used for the synthesis of Al-Ti-C composites is presented in Table 1. As a result of the synthesis, the initial samples transformed into quite strong and relatively dense compacts. During the work, the structure of the aluminum matrix composites was investigated after thermal synthesis, as shown in Figure 1. The results of quantitative analysis of the presented structural elements are provided in Table 2.

The results of the microstructural analysis (Fig. 1) revealed the presence of uniformly distributed light particles of reinforcing phase with varying dispersion and shape within the gray metallic matrix. The structure with gray regions surrounded by dispersed spherical particles is characteristic of samples with aluminum content ranging from 45% to 50%, which were mixed with consideration of titanium carbide stoichiometry (Fig. 1, b, c). In samples with the maximum carbon content and 20% aluminum, the light dispersed particles were evenly distributed throughout the volume and positioned quite densely to one another (Fig. 1, a).



a b

c

a - 20Al-16C-64Ti wt., %;
b – 45Al-11C-44Ti wt., %;
c – 50Al-10C-40Ti wt., %;

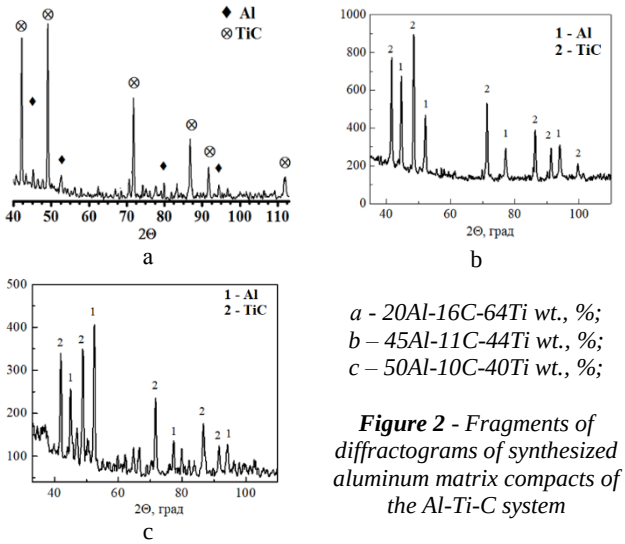
Figure 1 – SEM image of the Al-Ti-C ligature after synthesis

Quantitative analysis revealed that the gray regions in the microstructural photographs (Fig. 1) consist mainly of aluminum (Table 2, spectra 2 and 4) or a mixture of aluminum and titanium carbide particles (spectrum 6). The light rounded particles (spectra 1 and 3) correspond to a composition close to the stoichiometric ratio of titanium carbide. Furthermore, an increase in the aluminum content from 20 to 50% leads to the appearance of oxygen in the samples, with its percentage gradually increasing in the samples with a composition of 50Al-10C-40Ti (wt. %).

Table 2 *- Content (wt. %) of elements at various points in the synthesized Al-Ti-C composite compacts.*

Spectrum No	Al, %	Ti, %	C, %	O, %
1	3,714	78,336	17,950	
2	92,861	2,839	4,299	
3	30,33	60,36	9,3	-
4	55,1	44,1	3,86	-
5	15,48	47,01	24,26	13,25
6	30,91	26,18	31,36	11,55

The results of X-ray diffraction analysis are presented in Figure 2. After the reactive synthesis, the diffractograms of all samples show pronounced lines of titanium and aluminum carbide (Figure 2). Using the Rietveld method, the percentage content of the main phases in the different composition samples was determined (Table 3). It can be seen from Table 3 that the percentage content of aluminum and titanium carbide corresponds to the content of the main elements in the initial composite mixtures.



a b

c

a - 20Al-16C-64Ti wt., %;
b – 45Al-11C-44Ti wt., %;
c – 50Al-10C-40Ti wt., %;

Figure 2 *- Fragments of diffractograms of synthesized aluminum matrix compacts of the Al-Ti-C system*

Table 3 *- Influence of the content of main phases in aluminum matrix composites depending on the composition*

№	Composition	Content of Main Phases (%)	
		Al	TiC
1	20Al-16C-64Ti	15,3	84,7
2	45Al-44Ti-11C	40,8	59,2
3	50Al-40Ti-10C	45,1	54,9

The influence of copper addition on the structure, density, porosity, and hardness of the hot-stamped aluminum matrix composites with different compositions, specifically mixtures No. 2, 3, 5, and 6 (Table 1), was determined. The forging was also applied to synthesized aluminum matrix compacts of mixtures 1 and 4 on a hydraulic press, revealing that this technology and deformation scheme do not allow obtaining a dense composite. This can be attributed to the fact that composites with a high content of carbide phase, approximately 80 wt.% have low plasticity and, therefore, require higher deformation forces for complete densification and the production of a high-density compact.

Table 4 presents the density values of the aluminum matrix composite materials (AMCM) before and after forging, and the density of the composites was determined using the hydrostatic weighing method. Based on the provided table, it can be seen that copper alloying of aluminum-based composites, obtained under the specified conditions, negatively affects the final material's porosity. This dependence can be explained by the fact that these composites require higher deformation forces, specifically hot stamping with impact loading.

Table 4 *- Density and porosity values for AMCM before and after hot stamping at a preheating temperature of 530°C*

№	Composition, wt.%	γ, g/cm^3 theoretical	γ, g/cm^3 after forging	Porosity, %
1	45Al-11C-44Ti	3,19	3,09	3,1
2	50Al-10C-40Ti	3,14	3,22	0
3	45Al-5Cu-10C-40Ti	3,27	3,06	6
4	50Al-5Cu-9C-36Ti	3,22	2,71	15

However, despite the relatively high porosity of the 45Al-5Cu-10C-40Ti and 50Al-5Cu-9C-36Ti composites, they exhibit high hardness compared to samples without copper additions. As shown in Figure 3, the hardness of copper-alloyed composites increased from 62-80 HRB to 90-91 HRB. Copper is a well-known alloying element for aluminum alloys, which, in turn, positively influences the strengthening of the aluminum matrix in the composite and, consequently, the final hardness of the material.

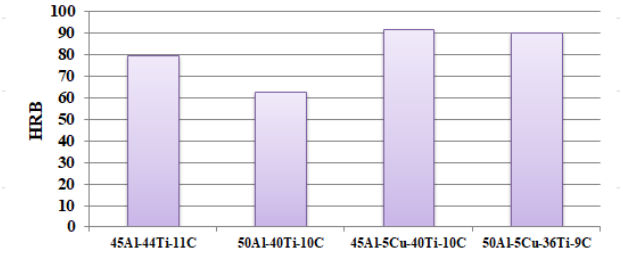
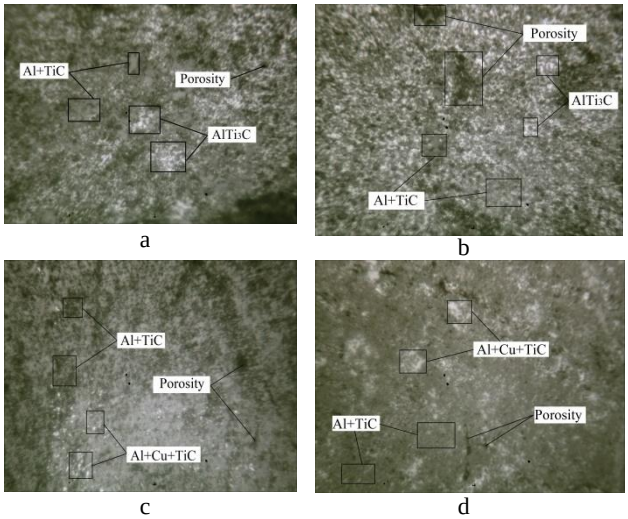


Figure 3 *– The influence of copper additives on the hardness of alumino-matrix composites*

The investigation of samples obtained after forging with various compositions has shown that the microstructure of the composites (Fig. 4) is characterized by the presence of two distinct phases: the matrix comprises aluminum with dispersed titanium carbide inclusions, and a small amount of the AlTi3C phase for

composites without copper alloying. The microstructure of copper-doped composites is somewhat different from the previous ones, namely, the presence of well-defined light inclusions (copper) in the material structure. There are also present two phases in the structure of these composites: the aluminum-based matrix with dispersed titanium carbide inclusions and the Al+Cu+TiC phase. Unfortunately, copper-doped phases are not completely evenly distributed over the structure of the composite, especially in the 45Al-5Cu-10C-40Ti sample, which may be due to an insufficient amount of the liquid phase, which leads to poor wetting of the carbide inclusions and the alloying element. Furthermore, Fig. 4 indicates the presence of pores in the structures of all composite compositions. But, in copper-alloyed samples, their quantity is slightly higher, and their size is smaller.



a - 45Al-11C-44Ti wt., %; b – 50Al-10C-40Ti wt., %;
c – 45Al-5Cu-10C-40Ti wt., %; d – 50Al-5Cu-9C-36Ti wt., %;

Figure 4 *- Microstructure of aluminum matrix composites after forging (x1000).*

4. Conclusion

1. The results of microstructural analysis of aluminum matrix synthesized composites showed the presence in the structure of light particles fairly evenly distributed in the gray metal matrix, which strengthen the phase of different dispersion and shape.

2. X-ray phase analysis demonstrated that after the reactive synthesis, all samples exhibited well-defined lines corresponding to titanium carbide and aluminum. Additionally, using the Rietveld method, the percentage content of the main phases in the composites was determined.

3.The influence of copper addition on the structure, density, porosity, and hardness of forging aluminum matrix composites with different compositions was investigated. It was found that copper alloying in the amount of 5 wt.% increases the hardness of aluminum matrix composites but negatively affects their porosity. However, this effect could also be attributed to insufficient deformation forces since these materials require higher deformation efforts, namely, forging with impact loading.

5. References

1. Frage N, Froumin N, Dariel MP. Wetting of TiC by non-reactive liquid metals. Acta Mater 2002;50(2):237-245.

2. Dezellus O, Eustathopoulos N. Fundamental issues of reactive wetting by liquid metals. J Mater Sci 2010;45(16):4256-4264.

3. Schwarz K. Band structure and chemical bonding in transition metal carbides and nitrides. Crit Rev Solid State 1987;13:211-257.

4. Contreras A, Angeles-Chavez C, Flores O, Perez R. Structural, morphological and interfacial characterization of Al–Mg/TiC composites. Mater Character 2007;58:685- 693.

5. Albiter A, Leon CA, Drew RAL, Bedolla E. Microstructure and heat-treatment response of Al-2024/TiC composites. Mater Sci Eng 2000;A289:109-115.

6. Karantzalis AE, Wyatt S, Kennedy AR. The mechanical properties of Al-TiC metal matrix composites fabricated by a flux-casting technique. Mater Sci Eng 1997;A237:200-206.

7. Clyne TW. Metallic composite materials. In: Cahn RW, Haasen YP, editors. Physical metallurgy. Amsterdam: Elsevier, 1996. p. 2568-2625.

8. Humphreys FJ, Basu A, Djazeb MR. The microstructure and strength of particulate metal-matrix composites. In: Proceedings of 12th Riso international symposium on materials science. Roskilde, September, 1991. p. 51-66.

9. McKimpson MG, Scott TE. Processing and properties of metal matrix composites containing discontinuous reinforcement. Mater Sci Eng 1989;A107:93-106.

10. Lloyd DJ. Aspects of fracture in particulate reinforced metal matrix composites. Acta Metall Mater 1991;39(1):59-71.

11. Jiang WH, Song GH, Han XL, He CL, Ru HC. Synthesis of TiC/Al composites in liquid aluminium. Mater Lett 1997;32:63-65.

12. Harata M, Choh T, Kobashi K. Effect of alloying elements on TiC particulate dispersion in aluminium matrix composites. J Japan Inst Metals 1990;54:1382-1391.

13. Stefanescu DM, Dhindaw BK. Principles of solidification – Behavior of insoluble particles at the solid/liquid interface. In: Thompson M, editor. Metals Handbook. Metals park: ASM Int, 1988. p.142-147. [16] Jin I, Lloyd DJ. Solidification of SiC particulate reinforced Al-Si alloy composites. In: Masounave J, Hamel FG, editors. Fabrication of particulates reinforced metal matrix composites. Materials Park: ASM Int, 1990. p.47-52.

14. Lloyd DJ, Lagace H, McLeod A, Morris PL. Microstructural aspects of aluminiumsilicon carbide particulate composites produced by a casting method. Mater Sci Eng 1989;A107:73-80.

15. Mortensen A. Interfacial phenomena in the solidification processing of metal matrix composites. Mater Sci Eng 1991;A135:1-11.

16. Selcuk C, Kennedy AR. Al–TiC composite made by the addition of master alloys pellets synthesized from reacted elemental powders. Mater Lett 2006;60:3364-3366.

17. Kennedy AR, Wyatt SM. The effect of processing on the mechanical properties and interfacial strength of aluminium/TiC MMCs. Compos Sci Technol 2000;60:307- 314.

18. Nukami T, Flemings MC. In-situ synthesis of TiC particulate-reinforced aluminum matrix composites. Metall Mater Trans 1995;A26(7):1877-1884.

19. Hashimoto S, Yamaguchi A, Koshino M. Fabrication and characterization of TiC:Al composites. Mater Sci Eng 1999;A265:71-76.

Optical Logic Half Adder Based On Multi Ring Resonators Silicon Photonic Crystal Structures

Moria Gulitski, Yonatan Pugachov, Omri Mizrahi, Dror Malka*
Faculty of Engineering, Holon Institute of Technology (HIT), Holon 5810201, Israel;
*Corresponding author drorm@hit.ac.il; Tel.: +972-3-502-6648

Abstract: *In this paper, we introduce an innovative design for an all-optical half adder (HA) utilizing a pair of dual-ring resonators within a 2-dimensional square lattice photonic crystal (PC) framework, all achieved without the use of nonlinear materials. The all-optical HA encompasses both AND and XOR gates, each constructed with cross-shaped waveguides and twin ring resonators positioned in a 2D square lattice PC. These resonators are filled with silicon (Si) rods set in a silica (SiO2) medium. Employing the plane-wave expansion (PWE) and finite difference time domain (FDTD) techniques, we comprehensively analyzed and simulated the behavior of the AND and XOR gates. The simulation outcomes reveal that the internal light propagation within the device emulates the functions of traditional AND and XOR gates. Consequently, the proposed device displays promising potential for integration into optical arithmetic logic units, thereby enhancing digital computing circuits.*

The structural configuration encompasses an optical AND gate and an optical XOR gate, meticulously designed to operate within the C-band spectrum. The results unequivocally demonstrate a distinct demarcation between logic states 1 and 0, encapsulating a narrow power range that contributes to heightened robustness and minimized logic errors within the photonic decision circuit. Hence, the proposed HA stands as a pivotal building block in the creation of cutting-edge photonic arithmetic logic units.

1. Introduction

Optical logic elements have garnered significant interest due to their robust capabilities in the realm of optical communication and their potential to advance computing methodologies, thereby enhancing signal processing within all-optical data networks [1-4].

All-optical logic elements hold promises for diverse networking applications [5-8], encompassing optical computing, addressing, signal rejuvenation, clock recovery, and error detection.

For the optimization of intricate logic components, the imperative lies in compact, rapid, and energy-efficient logic gates.

A spectrum of materials and techniques has been harnessed in the design of all-optical logic gates, incorporating waveguide interferometers, optical fibers [9-12], semiconductor optical amplifiers [13-18], and photonic crystals (PC) [19-25]. However, these materials and approaches are constrained by inherent limitations, such as dimensional bulk, restricted speed, and challenges in achieving chip-scale integration.

Particularly noteworthy is the confinement faced by fiber-based logic gates, which impedes their seamless chip-level integration. Meanwhile, semiconductor optical amplifiers grapple with the inevitable intrusion of spontaneous emission noise. In contrast, PC offers a potential remedy to these challenges, boasting straightforward architecture, ultracompact form, minimal power dissipation, and rapid operation. A PC square embodies a periodic dielectric nanostructure characterized by distinctive refractive indices that influence the propagation of electromagnetic waves within the configuration.

Research endeavors have delved into the refinement and enhancement of PC-based logic gates. A subset of these studies revolves around nonlinear optical phenomena [26], the self-collimation effect [27], multi-mode interferometry [28], PC ring resonators (RR) [29], and Y-shaped PC waveguides [30]. Notably, to date, no optical half-adder (HA) that leverages optical logic gates based on cross-shaped PC waveguides combined with RR has been proposed.

In this exposition, we unveil a novel configuration for an optical HA that obviates the need for nonlinear materials. The envisaged HA materializes through a symmetrical amalgamation of all-optical AND and XOR logic gates, founded upon cross-shaped PC waveguides and a pair of 2D PC RRs, constituted by cylindrical silicon (Si) rods embedded in silica (SiO2), thus engendering a shared full band gap. This proposed framework harbors substantial potential for integration into photonic integrated circuits. Time-domain simulations of electromagnetic wave propagation within the logic gates were executed via a two-dimensional finite difference time domain (FDTD) approach, while the photonic band gap (PBG) was assessed utilizing the plane wave expansion (PWE) method.

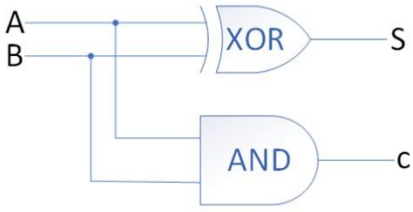
2. Principle and analysis

The PBG delineates the spectrum of frequencies within which the propagating wave within the structure encounters reflection. This phenomenon is vividly illustrated in the band structure, attainable through the application of the PWE principle and Maxwell's equations pertinent to transverse electric (TE) and transverse magnetic (TM) polarizations. These equations are numerically solved to address the ensuing expression:

$$\nabla \times \left(\frac{1}{\varepsilon_r} \nabla \times H(r) \right) = \left(\frac{\omega}{c} \right)^2 H(r) \quad (1)$$

Where H is the magnetic field, ε_r is the relative permittivity, ω is the angular frequency, and c is the speed of light. From the frequency range, we can calculate the range of wavelengths that should be used.

Generally, a HA consists of two logic gates XOR & AND. Figure 1 shows that the outputs of HA sum (S) & carry out (C) are identical to the outputs of two logic gates XOR & AND respectively for the respective inputs of A and B.



Inputs		Outputs	
A	B	S	C
0	0	0	0
0	1	1	0
1	0	1	0
1	1	0	1

(a) (b)

Figure 1 *– logic gates (a) and accuracy table (b) of a HA.*

The foundation of the optical logic HA configuration rests upon a pair of T-splitters, meticulously designed to partition the wave while minimizing power dissipation. These splitters collaborate harmoniously with XOR and AND logic gates, visually depicted in figure 2 (a). The graphical representation highlights red-hued regions corresponding to Si, juxtaposed with white regions signifying SiO2. In order to streamline the intricacies inherent in the elaborate optical HA showcased in figure 2(a), a strategic approach has been undertaken. Specifically, two distinct optical logic gates, namely AND and XOR, are introduced independently, both adhering to identical parameters intrinsic to the PC structure.

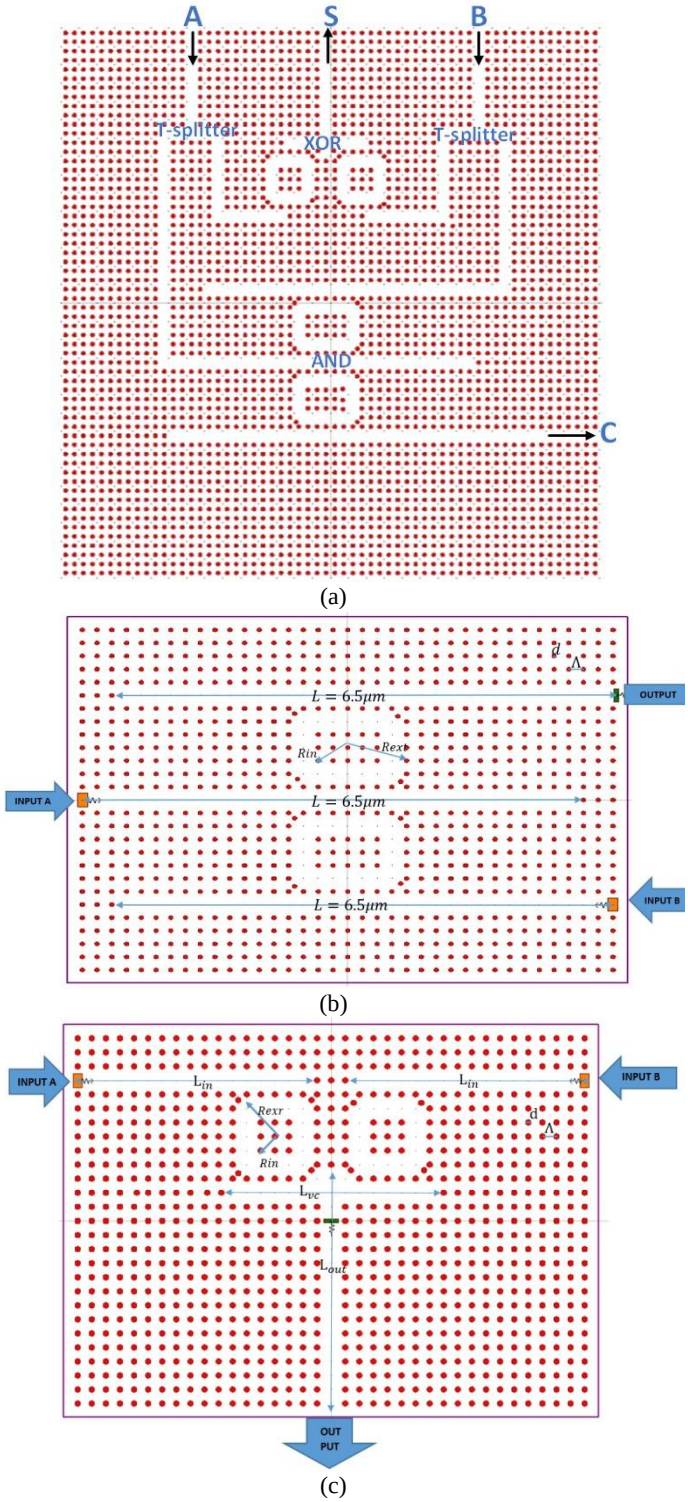


Figure 2 *- Schematic structures of proposed all-optical component: (a) HA. (b) AND gate. (c) XOR gate.*

Figure 2 (b) portrays the envisioned blueprint of an all-optical AND gate configuration. This assembly encompasses three parallel horizontal waveguides and a pair of RR. Each waveguide has an elongation (L) of 6.5 μm. The two RR exhibit uniform inner radius (Rin) of 0.6 μm and external radius (Rext) of 1.6 μm. These RR entities are strategically positioned amidst the two flanking waveguides. The initial RR is situated above input B, while the subsequent RR is aligned with input A. Manifesting two input ports and a solitary output port, the all-optical AND logic gate is realized.

Figure 2 (c) introduces the envisaged model of an all-optical XOR gate. This assembly encompasses three parallel horizontal waveguides, supplemented by a single vertical waveguide and a pair of RR. The upper horizontal waveguides extend a distance (Lin) of 9 μm, while the third horizontal waveguide (Lvc) spans 8 μm. Simultaneously, the vertical waveguide extends a length (Lout) of 6 μm. Like its predecessor, the RR maintains a consistent inner radius (Rin) of 0.5 μm and external radius (Rext) of 1.5 μm. These RR entities are situated beneath the input waveguides. Similar to the AND gate, the all-optical XOR logic gate showcases two input ports and a single output port.

Both logic gates exhibit cylindrical Si rods with a diameter (d) of 200 nm and a pitch (Λ) of 500 nm, as showcased in figures 2 (b-c). The adoption of this unique configuration in both logic gates is rooted in its ability to foster a complete TE band gap, aligned with an orthogonal magnetic field relative to the rods.

Figures 3 (a-b) provide insight into the refractive index profile of the logic gates. These representations feature two-dimensional cylindrical Si rods, distinguished by a refractive index of 3.5, coexisting harmoniously with the cover area and SiO2, both characterized by a refractive index of SiO2 equating to 1.45. This configuration materializes a comprehensive band gap at a wavelength of 1550 nm.

3. Simulation results

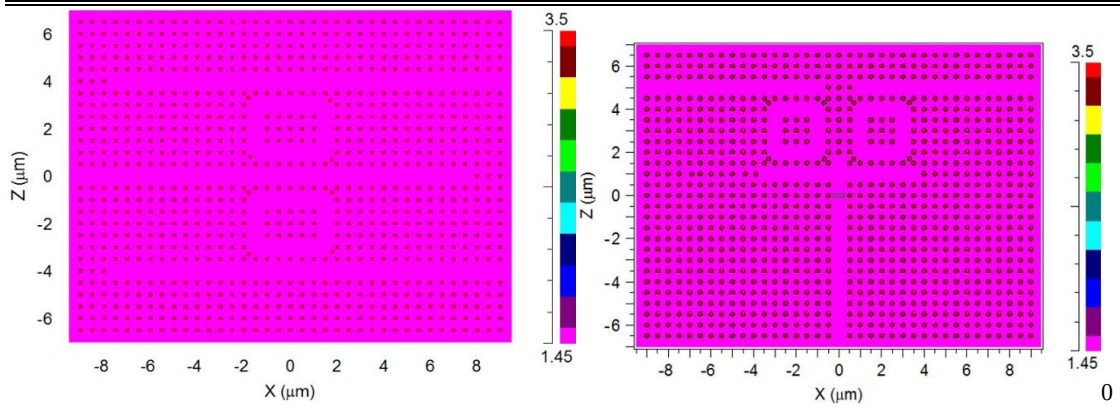
The simulation process and numerical optimization of the proposed all-optical logic gates XOR and AND are performed with Rsoft Photonics CAD Suite software, which uses the Band-Solve tool calculation method based on the PWE principle for solving the PBG. Whereas the Rsoft FULLWAVE tool, which uses the FDTD method, was applied for the simulation of the transmission diagram and reflection of optical power in the logic gates output.

The AND and XOR optical logic gates receive a Gaussian pulse at the input, which is used as an input signal in the simulations.

For locating and optimizing the PBG, and calculating the dispersion of defected states, testing only one small group of points in the first Brillouin zone (1BZ) is sufficient. A group of symmetrical points characterizes every crystalline structure, and to build a graph that describes the PBG it is essential to determine the points of symmetry in 1BZ and connect them with linear lines. Figures 4 (a-b) were extracted using the Band-Solve tool which shows the TE PBG for AND and XOR gates.

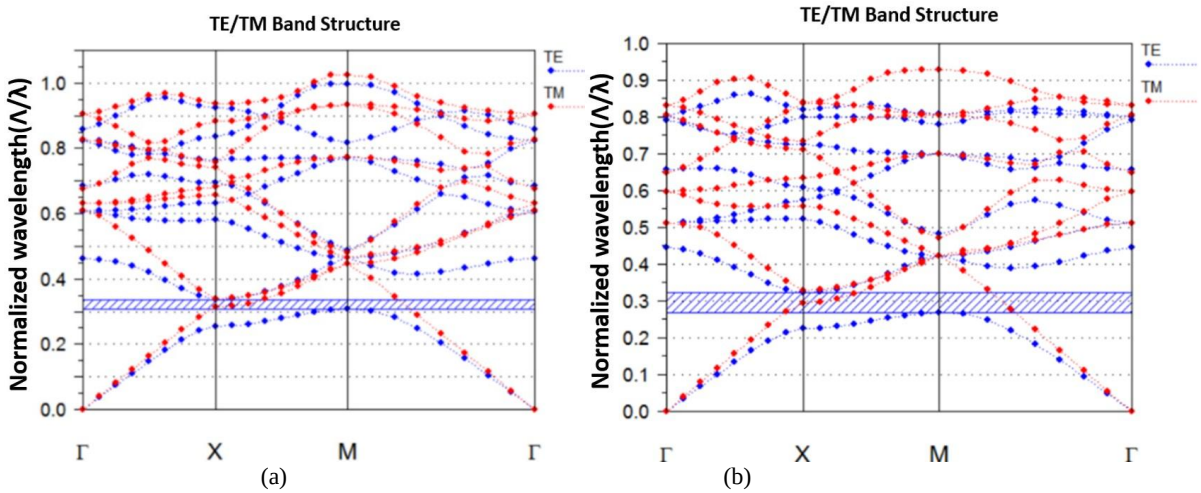
The bend diagram depicts that the PBG only shows in the TE polarization mode as expected by the special configuration of the HA and occurs in the range of $0.3 < \Lambda/\lambda < 0.34$ for the AND gate and $0.26 < \Lambda/\lambda < 0.33$ for the XOR gate. The wavelength range of the AND gate is $1470\ nm < \lambda < 1660\ nm$ and the wavelength range of the XOR gate is $1510\ nm < \lambda < 1920\ nm$, thus the common wavelength range is $1510\ nm < \lambda < 1660\ nm$. Therefore, the proposed design is suitable to the operated wavelength of 1550 nm and can function as well in the C-band spectrum (1540-1570 nm).

The FDTD simulations were optimized to select the best mesh convergence for the ideal x and z axis grid sizes of 10 nm. Figures 5(a-d) show the light propagation of the two input Gaussian pulses through the PC configuration of the optical AND gate for different logic states.



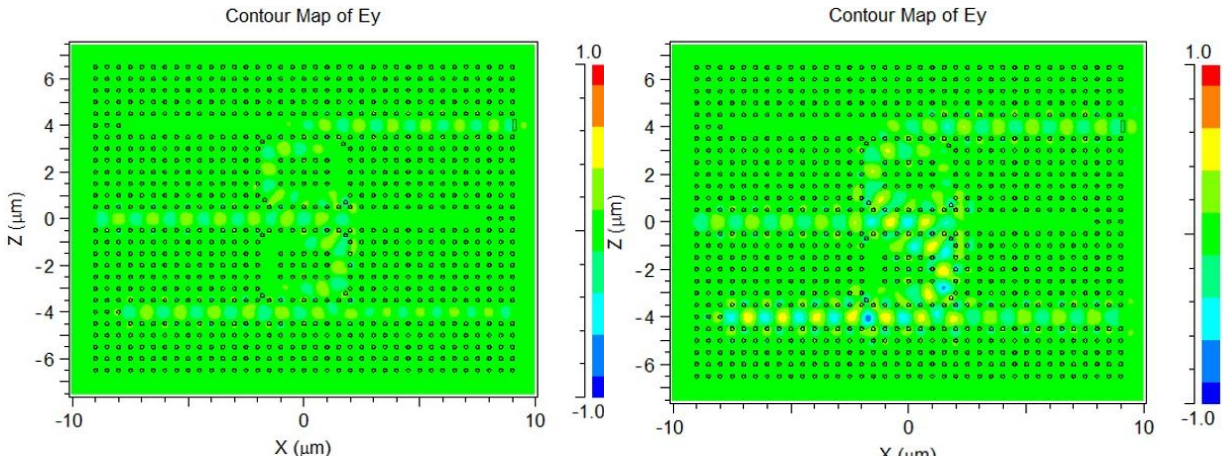
(a) (b)

Figure 3 *– Refractive index profile of the all-optical logic gates: (a) AND gate. (b) XOR gate.*

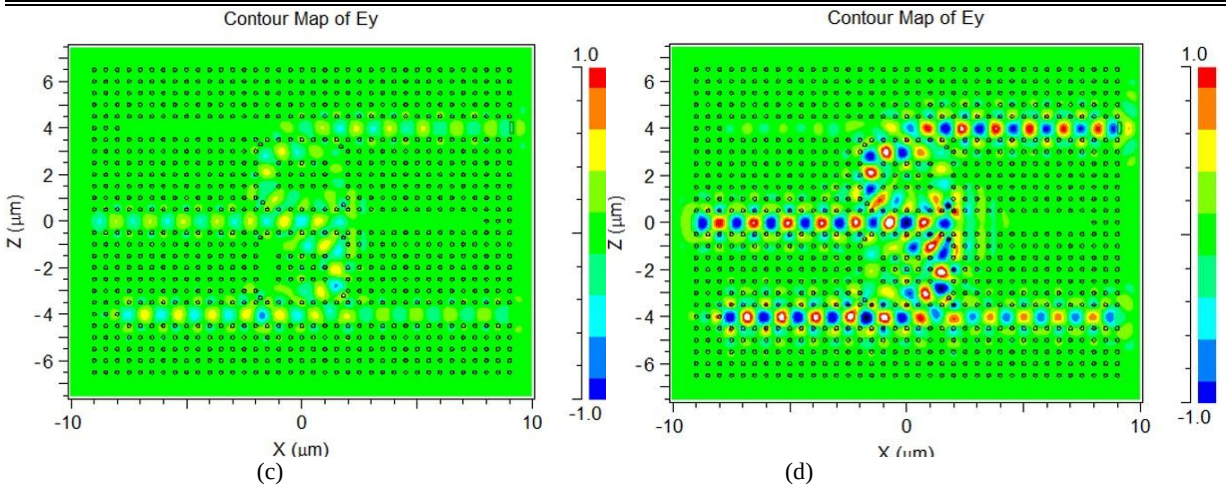


(a) (b)

Figure 4 *– Band diagram of all-optical logic gates: (a) AND. (b) XOR.*



(a) (b)



(c) (d)

Figure 5 *– Light intensity propagation profile of the Gaussian pulses at the x-z plane for AND PC gate with logic inputs: (a) 0-0. (b) 0-1. (c) 1-0. (d) 1-1.*

Figures 5 (a-d) show the transmission of the Gaussian signals through the PC configuration of the AND gate. The signals propagate through the two horizontal corresponding waveguides, the lower input signal couples to the corresponding RR and combines with the upper input signal. The combined signal couples to the other RR and continues to the output signal.

Figure 5 (a) represents the case where the input power of the Gaussian signals A and B is 0.1 W, the signals decay through the RR and a low-intensity signal travels through the output waveguide, the value of which is determined by the simulation result is 0.12 W.

Figure 5 (b) represents the case where the input power of the Gaussian signal A is 0.1 W and the input power of the Gaussian signal B is 0.9 W, the signals decay through the RR and a low-intensity signal travels through the output waveguide, the value of which determined by the simulation result is 0.17 W.

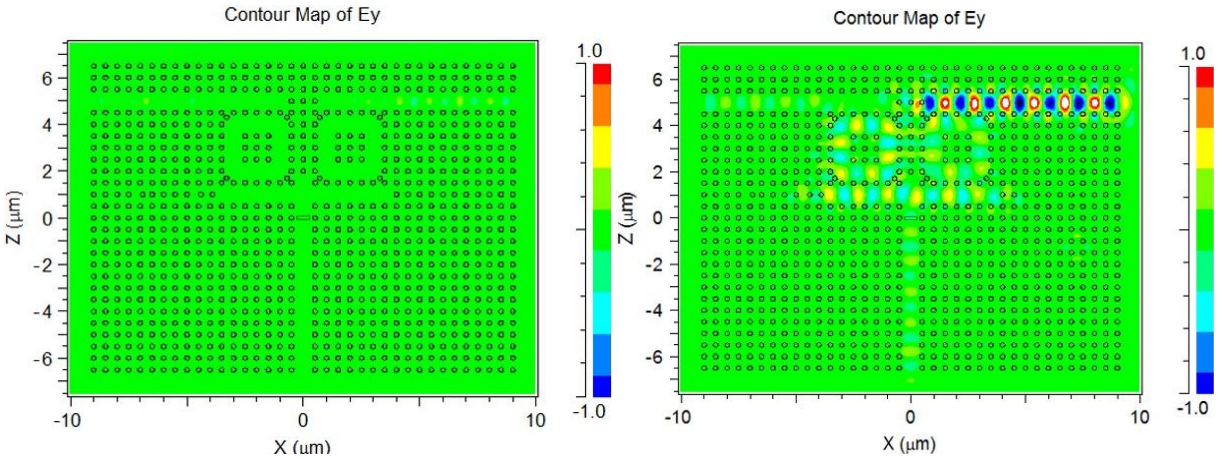
Figure 5 (c) represents the case where the input power of the Gaussian signal A is 0.9 W and the input power of the Gaussian signal B is 0.1 W, the signals decay through the RR and a low-intensity signal travels through the output waveguide, the value of which determined by the simulation result is 0.27 W.

Figure 5 (d) represents the case where the input power of the Gaussian signals A and B is 0.9 W, the signals amplify through the RR and a high-intensity signal travels through the output waveguide, the value of which is determined by the simulation result is 0.85 W.

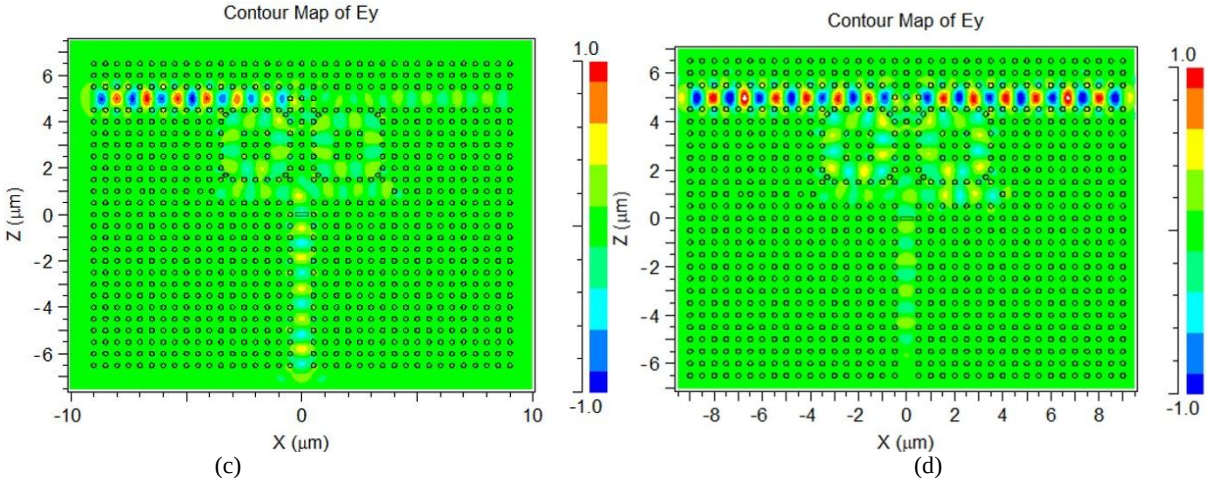
Table 1 *– Logic values of intensity at ports of AND gate with inputs: 0-0. 0-1. 1-0. 1-1.*

Input A (w)	Input A (logic)	Input B (w)	Input B (logic)	Output S (w)	Output S (logic)
0.1	0	0.1	0	0.12	0
0.1	1	0.9	0	0.17	0
0.9	0	0.1	1	0.27	0
0.9	1	0.9	1	0.85	1

Figures 6 (a-d) show the working state of the logic gate XOR for different states of inputs A and B.



(a) (b)



(c) (d)

Figure 6 *– Light intensity propagation profile of the Gaussian pulses at the x-z plane for XOR PC gate with logic inputs: (a) 0-0. (b) 0-1. (c) 1-0. (d) 1-1.*

Figures 6 (a-d) show the transmission of the Gaussian signals through the PC configuration of the XOR gate. The signals propagate through the two upper horizontal corresponding waveguides, then their energy is transferred by light coupling to the corresponding RR, which leads them to the T-combiner region, which combines the two signals into the output waveguide Lvc.

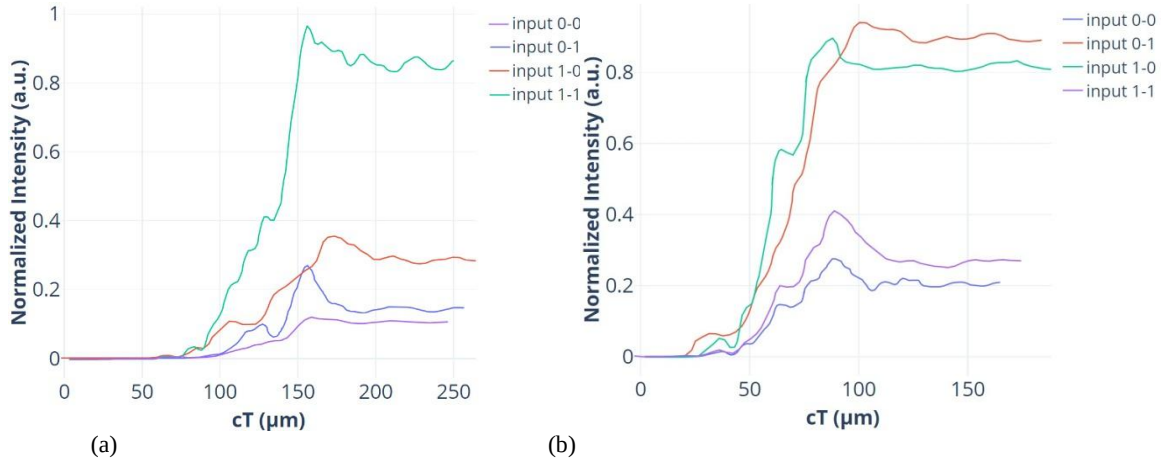
Figure 6 (a) represents the case where the input power of the Gaussian signals A and B is 0.1 W, the signals decay through the RR and a low-intensity signal travels through the output waveguide, the value of which, determined by the simulation result, is 0.2 W.

Figure 6 (b) represents the case where the input power of the Gaussian signal A is 0.1 W and the input power of the Gaussian signal B is 0.9 W, the signals amplify through the RR and a high-intensity signal travels through the output waveguide, the value of which, determined by the simulation result, is 0.9 W.

Figure 6 (c) represents the case where the input power of the Gaussian signal A is 0.9 W and the input power of the Gaussian signal B is 0.1 W, the signals amplify through the RR and a high-intensity signal travels through the output waveguide, the value of which, determined by the simulation result, is 0.81 W. Figure 6 (d) represents the case where the input power of the Gaussian signals A and B is 0.9 W, the signals decay through the RR and a low-intensity signal travels through the output waveguide, the value of which, determined by the simulation result, is 0.26 W.

Table 2 *– Logic values of intensity at ports of XOR gate with inputs: 0-0. 0-1. 1-0. 1-1.*

Input A (w)	Input A (logic)	Input B (w)	Input B (logic)	Output S (w)	Output S (logic)
0.1	0	0.1	0	0.2	0
0.1	1	0.9	0	0.9	1
0.9	0	0.1	1	0.81	1
0.9	1	0.9	1	0.26	0



(a) (b)

Figure 7 *– Light intensity diagram for (a) AND gate, (b) XOR gate with inputs: 0-0, 0-1, 1-0, 1-1.*

The stabilization time can be described as the time it takes for the signal at the output port of a logic gate to reach a stabilized state of intensity, such that a logic state can be determined. Figure 7 (a) represents the light intensity at the output as a function of time for AND gate for the different states of inputs A and B. Figure 7 (b) represents the light intensity at the output as a function of time for the XOR gate for the different states of inputs A and B. The stabilization time for each logic gate can be determined from the previously mentioned figures. The stabilization time for the AND gate is 0.66 psec and for the XOR gate is 0.4 psec.

The stabilization intensity is the normalized intensity of the signal at the output of the logic gate when the stabilization time is reached. Figure 7 (a) shows the stabilization intensity for AND gate for the different states of inputs A and B. When the input is A = 0, B = 0 the normalized intensity is greater than 11% and reaches 13%, and the stabilization intensity is 12%. When the input is A = 0, B = 1 the normalized intensity is greater than

16% and reaches 27%, and the stabilization intensity is 17%. When the input is A = 1, B = 0 the normalized intensity is greater than 26% and reaches 37%, and the stabilization intensity is 27%. When the input is A = 1, B = 1 the normalized intensity is greater than 83% and reaches 98%, and the stabilization intensity is 85%.

Figure 7 (b) shows the stabilization intensity for the XOR gate for the different states of inputs A and B. When the input is A = 0, B = 0 the normalized intensity is greater than 19% and reaches 27%, and the stabilization intensity is 20%. When the input is A = 0, B = 1 the normalized intensity is greater than 85% and reaches 93%, and the stabilization intensity is 90%. When the input is A = 1, B = 0 the normalized intensity is greater than 80% and reaches 91%, and the stabilization intensity is 81%. When the input is A = 1, B = 1 the normalized intensity is greater than 24% and reaches 40%, the stabilization intensity is 26%.

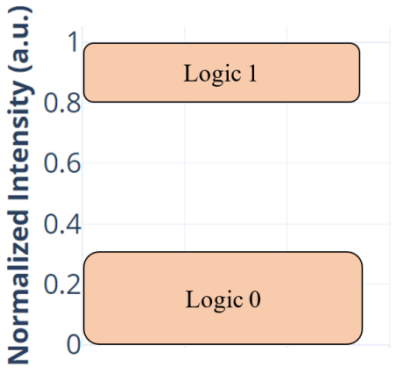


Figure 8 *– Logic state range by a function of light intensity.*

Figure 8 is based on the results of the light intensity at the output of the XOR gate and AND gate for the different states of inputs A and B shown in figures 7 (a-b). The logic ranges were determined by the point on the graph where the normalized intensity fluctuates around the same point and settles into a stabilized state.

Logic 0 is defined between 0 to 0.27 normalized intensity, and logic 1 is defined between 0.81 to 1 normalized intensity. Thus, the device has a narrow power range that can be utilized to define better the separation between 0 and 1 logic states.

In table 3 a comparison was shown between the HA design introduced above, and other HA structures previously proposed in published papers. As shown in table 3 the main characteristics of the HA are stabilization time, logic state 0 range, and logic state 1 range, and dimensions were compared. All compared HA devices function at the C-band spectrum.

From table 3 it can be concluded that the main benefit of the proposed design is the small logic state range in comparison to other HA devices. This means that our device has the best stability to deal with logic errors that can happen in the detection system.

Table 3 *– Comparison between the main characteristics of different HA structures.*

Half adder type	Stabilization time (psec)	Logic state 0 range (W)	Logic state 1 range (W)	Dimensions (μm) (Length x width)	Year
2D photonic crystals [31]	-	0 – 0.4	0.6 – 1	12.16 x 11.08	2016
Photonic crystal T-shaped waveguides [32]	0.485	0 – 0.2	0.5 – 1	23.4 x 25.8	2017
2D Photonic crystals multi resonance effect [33]	0.087	0 – 0.35	0.5 – 1	5.94 x 8.1	2020
Ultra-compact photonic crystal [34]	1.05	0 – 0.2	0.6 – 1	19.8 x 23.4	2021
Photonic Crystal Multi Ring Resonator [35]	0.66	0 – 0.2	0.8 – 1	30 x 30	2023

4. Conclusion

This study introduces an innovative paradigm, outlining a pioneering design that amalgamates all-optical AND and XOR gates, seamlessly integrated within an all-optical half-adder (HA) configuration. This unique setup harnesses a specialized architecture founded on Photonic Crystal Ring Resonators (PCRR), strategically situated within a two-dimensional square lattice structure, all while circumventing the need for nonlinear materials.

Employing the Rsoft Photonics CAD Suite software, the Band-Solve tool calculation method is employed, relying upon the foundational principles of Plane Wave Expansion (PWE) and Maxwell's equations. This computational framework elucidates the structure's operational range, effectively pinpointing the wavelengths at which the AND and XOR gates function optimally within the C-band spectrum.

Validation and scrutiny of the proposed design are facilitated through the Finite-Difference Time Domain (FDTD) method. This simulation imparts the transmission diagram and optical intensity at the output of the logic gates. These analyses demonstrate the distinct intervals characterizing logic state 0 (ranging from 0 to 0.3 normalized intensity) and logic state 1 (ranging from 0.8 to 1 normalized intensity). The overarching stabilization period culminates at a mere 0.66 picoseconds.

Integral to the proposed HA design is its intrinsic capacity to confer a lucid demarcation between logic states 1 and 0, achieved within a remarkably narrow power range. This advantageous attribute contributes to the minimization of potential logic errors in the photonic decision circuit.

An additional salient feature is the HA's dual-gate construction, a facet that ushers in the potential for expansive integration onto a grand-scale all-optical chip. This mirrors the CMOS chip design ethos, where logic gates form the elemental building blocks of intricate components. Such a configuration readily lends itself to seamless integration with existing CMOS standard-made chips and components. Furthermore, it serves as a foundational cornerstone for a photonic arithmetic logic unit, encapsulating the quintessence of chip-based photonic computation.

This pioneering HA design does not solely confine itself to classical computing; its applicability extends to the realm of quantum computing. Here, it can serve as a linchpin for photonic and quantum computing calculations, thereby further augmenting its versatile utility.

References

1. E. Cohen, D. Malka, A. Shemer, A. Shahmoon, Z. Zalevsky, and M. London, "Neural networks within multi-core optic fibers" Scientific Reports (2016).
2. B. Baruch Ben Zaken, T. Zanzury, and D. Malka, "An 8-Channel Wavelength MMI Demultiplexer in Slot Waveguide Structures" Materials. 9(11), 881 (2016).
3. N. Katash, S. Khateeb, and D. Malka "Combining Four Gaussian Lasers Using Silicon Nitride MMI Slot Waveguide Structure" Micromachines. 13(10), 1680 (2022).
4. R. Dadabayev, N. Shabairou, Z. Zalevsky, D. Malka “A visible light RGB wavelength demultiplexer based on

silicon-nitride multicore PCF" Opt. & Laser Tech. 111, 411-416 (2019).
5. N. A. Shalmany, A. G. Pour Rahbar, "On the choice of all-optical switches for optical networking" IEEE, (2007).
6. R. A Barry, V. W. S. Chan, K. L. Hall, E. S. Kintzer, J. D. Moores, K. A. Rauschenbach, E. A. Swanson, L. E. Adams, C. R. Doerr, S. G. Finn, H. A. Haus, E. P. Ippen, W. S. Wong, M. Haner "All-Optical Network Consortium-ultrafast TDM networks" IEEE, 14(5), 999–1013 (1996).
7. J. M. Lukens, H. H. Lu, B. Qi, P. Lougovski, A. M. Weiner, B. P. Williams "All-Optical Frequency Processor for Networking Applications" IEEE. 38(7) 1678-1687 (2020).
8. Y. Ji, H. Wang, J. Cui, M. Yu, Z. Yang, and L. Bai "All-optical signal processing technologies in flexible optical networks" Photonic Network Communications 38, 14–36 (2019).
9. P. St. J. Russell, "Photonic-crystal fibers, " J. Lightwave Technol. 24, 4729-4749 (2006).
10. T. A. Birks, J. C. Knight, and P. St. J. Russel, "Endlessly single-mode photonic crystal fiber," Opt. Lett. 22, 961-963 (1997).
11. J. Broeng, D. Mogilevstev, S. E. Barkou, and A. Bjarklev, "Photonic crystal fibers: A new class of optical waveguides," Opt. Fiber Technol. 5, 305-330 (1999).
12. P. Polishuk, "Plastic optical fibers branch out", IEEE. 44(9), 140-148 (2006).
13. K.E. Stubkjaer, "Semiconductor optical amplifier-based all-optical gates for high-speed optical processing".IEEE 6(6), 1428-1435 (2000).
14. T. Akiyama, M. Sugawara, Y. Arakawa, "Quantum-Dot Semiconductor Optical Amplifiers", IEEE 95(9), 1757-1766 (2007).
15. Armstrong, I. and Andonovic, I. and Kelly, A. E., "Semiconductor optical amplifiers: performance and applications in optical packet switching", Journal of Opt. Networking 3(12), 1536-(2004).
16. A. Sharaiha, J. Topomondzo, P. Morel, "All-optical logic AND–NOR gate with three inputs based on cross-gain modulation in a semiconductor optical amplifier", Optics Communications 265(1), 322-325(2006).
17. X. Zhang, S. Thapa and N. Dutta, "All-optical XOR gates based on dual semiconductor optical amplifiers" Cogent Physics, 6(1), (2019).
18. P. Urquhart, O. G. Lopez, G. Boyen, A. Bruckmann, "Optical Amplifiers for Telecommunications", IEEE, (2007).
19. D. Elbaz, D. Malka, and Z. Zalevsky, " Photonic crystal fiber based 1xN intensity and wavelength splitters/couplers, "Electromagnetics 32, 209–220 (2013).
20. D. Malka, Y. Sintov and Z. Zalevsky, "Fiber-laser monolithic coherent beam combiner based on multicore photonic crystal fiber, " Opt. Eng. 54(1), 011007-1-011007-5 (2014).
21. D. Malka and A. Peled, "Power splitting of 1 × 16 in multicore photonic crystal fibers" Applied Surface Science 417, 34 - 39 (2017).
22. D. Malka and G. Katz, "An Eight-Channel C-Band Demux Based on Multicore Photonic Crystal Fiber" Nanomaterials 8(10), 845 (2018).
23. D. Malka, E. Cohen, and Z. Zalevsky, "Design of 4 × 1 Power Beam Combiner Based on MultiCore Photonic Crystal Fiber" Appl. Sci. 7(7), 695 (2017).
24. O. Katz and D. Malka, "Design of novel SOI 1 × 4 optical power splitter using seven horizontally slotted waveguides" Photonics and Nanostructures - Fundamentals and Appl. 25, 9 - 13 (2017).
25. D. Malka and Z. Zalevsky, "Multicore Photonic Crystal Fiber Based 1x8 Two-Dimensional Intensity Splitters/Couplers," Electromagnetics 33, 413–420 (2013).
26. K. Singh, G. Kaur, "Interferometric architectures based All-Optical logic design methods and their implementations", Optics & Laser Tech., 69, 122-132(2015).
27. A. Sharma, K. Goswami, H. Mondal, T. Datta & M. Sen, "A review on photonic crystal based all-optical logic decoder: linear and nonlinear perspectives", Optical and Quantum Electronics 54(90), (2022).
28. Jiao SM, Liu JW, Zhang LW, Yu FH, Zuo GM, "All-optical logic gate computing for high-speed parallel information processing." Opto-Electron Sci 1, (2022).
29. H. M.E. Hussein, T. A. Ali, N. H. Rafat "A review on the techniques for building all-optical photonic crystal logic gates", Optics & Laser Tech., 106, 385-397(2018).
30. Y. Chen, Y. Cheng, R. Zhu, F. Wang, H. Cheng, Z. Liu, C. Fan, Y. Xue, Z. Yu, J. Zhu, X. Hu, and Q. Gong, "Nanoscale all-optical logic devices", Science China Physics, Mechanics & Astronomy, 62, 44201(2019).
31. Mohammad Mehdi Karkhanehchi, Fariborz Parandin, Abdulhamid Zahedi, "Design of an all optical half-adder based on 2D photonic crystals", Springer Science+Business Media New York (2016).
32. Enaul Haq Shaik, Nakkeeran Rangaswamy, "Implementation of photonic crystal based all-optical half adder using T-shaped waveguides", 2nd International Conference on Computing and Communications Technologies (ICCCT), (2017).
33. B.Elizabeth Caroline, M. Margarat, J. Vidhya, D. Purushothaman, R. Jayasri, "Design of Superficial Half Adder with 2D Photonic Crystals Multi Resonance Effect", 7th International Conference on Smart Structures and Systems (ICSSS), (2020).
34. Ali Lalbakhsh, Fariborz Parandin, Reza Kamarian, Mohamadreza Jomour, Mohammad Alibakhshikenari, "Ultra-compact Photonic Crystal Based All Optical Half Adder", Photonics & Electromagnetics Research Symposium (PIERS), (2021).
35. P.Yonatan, M. Gulitski, O. Mizrahi, D Malka. 2023. "Design of All-Optical Logic Half-Adder Based on Photonic Crystal Multi-Ring Resonator" *Symmetry* 15, no. 5: 1063.

The possibility of optimizing the properties of materials by using carbon nanostructures

Halina Yu. Mykhailova
G. V. Kurdyumov Institute for Metal Physics of the N.A.S. of Ukraine
36 Academician Vernadsky Boulevard, UA-03142 Kyiv, Ukraine
E-mail: mihajlova.halina@gmail.com

Abstract: *Carbon nanomaterials occupy one of the leading places in many areas of technology aimed at creating new materials and solving a number of problems for various industrial needs, including materials needed for alternative energy. The development of humanity is accompanied by a constant increase in resource availability, which, despite the discovery of new deposits of fossil resources, can lead to a shortage of energy resources. Therefore, in the modern world, it is necessary to develop technologies that will promote the use and implementation of non-traditional alternative energy sources.*

Introduction

Carbon nanomaterials occupy one of the leading places in many areas of technology aimed at creating new materials and solving a number of problems for various industrial needs, including materials needed for alternative energy.

The development of humanity is accompanied by a constant increase in resource availability, which, despite the discovery of new deposits of fossil resources, can lead to a shortage of energy resources. Therefore, in the modern world, it is necessary to develop technologies that will promote the use and implementation of non-traditional alternative energy sources.

The search for new materials and the study of their properties has always been and will be a priority direction in the development of science. Often, only new material makes it possible to solve questions that were considered unsolvable before its discovery. Targeted acquisition of new materials is a difficult task, often new materials are discovered by accident, and in this case, the first place is the study of their properties and the determination of possible areas of their application [1, 2].

For more than 30 years, carbon nanotubes (CNTs) have attracted the attention of scientists from many countries around the world. Such interest is caused by their unusual properties: they combine high strength and elasticity, thermal and electrical conductivity. Mechanical deformation and defects affect the electronic structure, concentration of charge carriers, electrical, emission, and other properties of CNTs. Defects occur both in the process of synthesis (growth and gas impurities) of CNTs, and in the event of external influences, especially radiation exposure. They deviate the shape of CNTs from a straight line, change the current flow conditions, affect the concentration of charge carriers, the Fermi energy, and electrical conductivity. The geometry of CNTs changes under the action of elastic deformation, which can significantly deform the profile of the entire nanotube, or locally in the region of the intersection of contacting nanotubes, which affects the electronic structure at the place of deformation, which controls the electrical conductivity of not only one nanotube, but also the entire array of CNTs. Considerable attention to radiation defects arose when finding out the possibility of using nanotubes in space and nuclear reactors. Research in this direction is also important for the use of high-energy irradiation as a technological tool for creating radiation defects and obtaining material with fundamentally new properties. However, information about the nature of radiation-stimulated effects in nanoobjects is still limited, since the influence of radiation defects on the properties of nanomaterials is currently little studied and, mainly, simulation results are published.

One of the promising directions for obtaining materials with specified properties is the development of composite materials modified with carbon nanostructures, which are introduced into it by mixing and uniform dispersion at the micron level.

Adding a small amount of CNTs to the dielectric matrix contributes to the appearance of electrical conductivity [3-8], the value of which has a wide range. This disparity in electrical conductivity is reflected by the complex interaction of various factors, the most important of which are the inherent conductivity of CNTs and their contact resistance.

The electrical conductivity of individual BWNTs is 10^4-10^7 $(\Omega \cdot m)^{-1}$ [9-11], the measured contact resistance for a SWNT beam is 100-400 kΩ for metal/metal or semiconductor/semiconductor compounds and twice as much as for metal/semiconductor systems [12].

Materials with higher strength, modulus of elasticity, and electrical conductivity are needed by the aviation and space industries, energy, transport, medicine, machine and instrument construction, etc. fields of science and technology. Nanostructured composite materials satisfy all these needs.

Composite materials are characterized by adjustable anisotropy and a gradient structure of properties, which is possible due to the directional orientation of fibers in the matrix, which is possible only when using powder technologies.

Nanofibers and nanorods, carbon nanotubes, metal, oxide and hydroxide nanotubes, nanoparticles of irregular or spherical shape, including particles of metals and alloys are used as nano-sized fillers of composite nanomaterials.

Most of the published works [4, 6, 7-9, 13-21] are devoted to composites with a polymer matrix, there are significantly fewer works with a metal matrix.

The main factors affecting the properties of metal-matrix composites reinforced with CNTs: differences in the properties of CNTs; difficulty of splitting agglomerates and uniform distribution of CNTs in the metal; the problem of compacting a mixture of metal powder and CNT; a wide variation in the ratio of the length to the diameter of the CNT (form factor); the possibility of chemical reactions between carbon and metal leading to the formation of carbides [21]. Sintering, high-temperature (one-sided) or isostatic (all-round) pressing, extrusion, high-temperature rolling, etc. are used to compact metal-CNT composites. [22]. However, all these processes take place at high temperatures, so low-temperature methods of compacting nanocomposites, for example, intensive plastic deformation, are preferred [22]. Copper composites with CNTs obtained in this way [23, 24] have significant differences in microstructure and microhardness from pure copper without CNTs.

Experiment

The electrical conductivity was was measured by the method described in [25].

Nanosystems consisting of $LaNi_5$ metal particles with different concentrations of CNTs were used to study the conductive properties. $LaNi_5$ microparticles were obtained by electric discharge in toluene. The $LaNi_5$-CNT nanosystem was obtained by mechanical mixing of the initial components in a certain proportion by 2 hours.

Multilayer nanotubes (diameter 10±2 nm) were obtained by chemical vapor deposition (CDV). The work function of microparticles of $LaNi_5$ is φ=3.6 eV, CNT – φ=4.7 eV.

Results

Electron microscopic images of multilayered carbon nanotubes presented on fig. 1. Al_2O_3-Fe_2O_3-MoO_3 catalyst particles are observed at the ends of CNTs, the average diameter of CNTs is 10±2 nm, observed CNTs in the range of diameters from 4 to 16 nm.

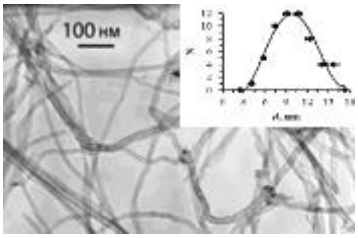


Fig. 1 – TEM image of multilayer carbon nanotubes

The initial value of electrical conductivity was recorded at densities ρ_0=2.72 g/cm^3, ρ_0=0.80 g/cm^3, ρ_0=0.10 g/cm^3 for $LaNi_5$, LaNi5 with 20 wt. % of CNTs and pure CNTs (Table 1).

Table 1. Electrophysical parameters of the studied composites $LaNi_5$+CNT

	$LaNi_5$+51 wt. % CNT d=28 μm	$LaNi_5$+ 20 wt.%CNT d=40 μm	$LaNi_5$+15 wt. % CNT d=135 μm
ρ_0, g/cm^3	0.11	0.8	0.88
σ_0, (Ohm·cm)$^{-1}$	10^{-5}	$4\cdot10^{-5}$	$3\cdot10^{-5}$
σ_{max}	10.65	13.18	13.55

When the piston is slightly lowered, σ(ρ) increases by 6 orders of magnitude due to rearrangement, densification, and an increase in the total contact area between neighboring particles of $LaNi_5$, $LaNi_5$ and CNTs, and CNTs among themselves. Upon further compression of the powder samples, σ(ρ) continues to increase smoothly for $LaNi_5$ and $LaNi_5$ nanocomposites with CNTs, while it remains practically unchanged for pure CNTs.

With an increase in particle size, an increase in electrical conductivity is observed by an order of magnitude at a lower concentration of CNTs: for 135 μm this is reflected at 15 wt. %, and for 28 μm at 51 wt. %. Significant increase in electrical conductivity is due to the transition of electrons from metal particles to CNTs: the latter is characterized by a low concentration of conduction electrons (n_e=1.3·10^{19} cm^{-3}) with high mobility (μ_{CNTs}~10 m^2/V·s) [26], while metals have a high concentration of electrons (~10^{22}) with very low mobility (for $LaNi_5$ μ=0.0072 m^2/V·s). These parameters are key in determining electrical conductivity (σ=*en*μ).

During the contact of metal particles of $LaNi_5$ with CNTs ($\varphi_{LaNi5}<\varphi_{CNTs}$), electrons will pass from the metal to CNTs (fig. 2) and increase their concentration in the latter. According to [27], mobility decreases by μ~1/n$^{1/2}$ as the concentration of charge carriers increases. Therefore, the current density (electrical conductivity) will increase ~n$^{1/2}$. An increase in the concentration of current carriers in CNTs due to charge transfer from the metal should lead to an increase in electrical conductivity. An increase in electrical conductivity by an order of magnitude during the establishment of electrical contacts between CNTs and metal is observed only at a certain concentration of CNTs.

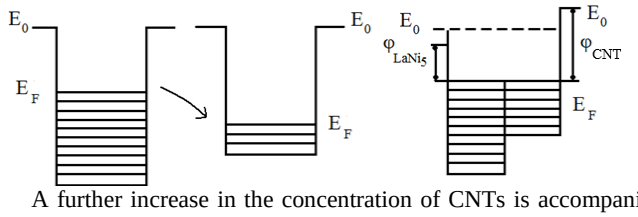
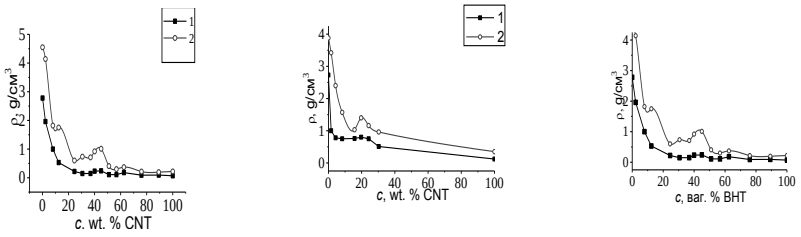


Fig. 2 – Energy diagram of metal-carbon nanotube contact

A further increase in the concentration of CNTs is accompanied by a value of electrical conductivity, which indicates a change in the efficiency of the transfer process.



a *b* *c*

Fig. 3 – Dependence of the density of the transition to the conducting state and the relaxation transition in the mechanical mixture on the concentration of CNTs. $LaNi_5$ particle size 28±6 μm (*a*), $LaNi_5$ particle size 40±10 μm (*b*), $LaNi_5$ particle size 135±13 μm (*c*). ■ is the density of the transition to the conducting state, ○ - the relaxation transition

In fig. 3 shows the dependence of the density of the transition to the conducting state and the relaxation transition of the mechanical mixture $LaNi_5$+ *c* wt. % of CNTs from the concentration of CNTs. When adding 2 wt. % CNT to powdered $LaNi_5$ transition to the conductive state decreases by 2-3 times (Fig. 3). Strongly anisotropic nanotubes, along the axis of which the current mainly flows, connect the particles together and thus reduce the density of the transition to the conducting state, while σ does not change significantly. On the curves ρ_0(c) and ρ_{rel}(c), maxima are observed at 51, 20, and 15 wt. % CNTs, as in the electrical conductivity curve, but not so sharp (Fig. 3). At higher concentrations of CNTs, the transition to the conducting state and the relaxation transition decrease, as a result of a certain destruction of order, an increase in elasticity, and a significant decrease in electrical conductivity. The small maximum of both transitions at the specified concentrations is associated with a slight ordering of CNTs in the composite, obviously, with an increase in the concentration of electrons in CNTs. Therefore, it is no coincidence that all three maxima on different curves of σ(*c*), ρ_0(*c*) and ρ_{rel}.(*c*) are observed at the same concentration (51 wt. %, 20 wt. %, and 15 wt. % of CNT), which may indicate the relationship of various physical parameters presented in Fig. 3 and Table 1.

Conclusions

When metal particles with a lower work output than the work output of nanotubes are added to CNTs, the radial electrical conductivity increases by more than an order of magnitude as a result of the transition of electrons from metal to CNTs, the mobility of which is greater than in metals, which leads to Coulomb interaction between various components and ordering of the system.

A maximum of electrical conductivity appears at 51, 20, and 15 wt. % CNT, the value of which exceeds the electrical conductivity of nanotubes by up to 20 times. This effect occurs as a result of the arrangement of the nanosystem when the Coulomb attraction between metal particles and CNTs is established, which leads to their sticking together and compacting. The mechanism of the effect is explained by the maximum increase in the concentration of conduction electrons in nanotubes when they are transferred from the metal, which occurs at certain concentrations of CNTs.

References

1. Elementi fiziki poverhni, nanostruktur i tehnologij [Pogosov V.V., Kunickij Yu.A., Babich A.V., Korotun A.V.]. – Zaporizh.: ZNTU, 2010. – 365 p.
2. Mikhailova G.Yu., Nishchenko M.M., Pimenov V.N., Starostin E.E., Tovtin V.I. Thermoelectric and Elastic Properties of Carbon Nanotubes Irradiated with High-Energy Electrons *Inorganic Mater.: Appl. Res.*V. 10.No. 5. 2019.P. 1052. https://doi.org/10.1134/S2075113319050186
3. Zhen Yao, Henk W. Ch. Postma, Leon Balents, Cees Dekker Carbon nanotube intramolecular junctions // Nature. – 1999. – V. 402. – P. 273-276.
4. Seamus A. Curran, Jamal Talla, Sampath Dias, Donghui Zhang, David Carroll Electrical transport measurements of highly conductive carbon nanotube/poly (bisphenol A carbonate) composite // Journal of applied physics. – 2009. – V. 105. – P. 073711-073718.
5. K. Ahmad, W. Pan, S.L. Shi Electrical conductivity and electrical properties of multiwall carbon nanotubes and alumina composities // Applied Physics Letters. – 2006. – V. 89. – P. 133122-133128.
6. J.K.W. Sandler, J.E. Kirk, I.A. Kinloch, M.S.P. Shaffer, A.H. Windle Ultra-low electrical percolation threshold in carbon-nanotube-epoxy composites // Polymer. – 2003. – V. 44**.** – P. 5893-5899.
7. M.B. Bryning, M.F. Islam, J.M. Kikkawa, A.G. Yodh Very low conductivity threshold in bulk isotropic single-walled carbon nanotube-epoxy composites // Advanced Materials. – 2005. – V. 17. – P. 1186-1191.
8. E. Kymakis, I. Alexandou, G.A. Amaratunga Single-walled carbon nanotube-polymer composites: electrical, optical and structural investigation // Synthetic Metals. – 2002. – V. 127. – P. 59-62.
9. M.B. Bryning, D.E. Milkie, M.F. Islam, J.M. Kikkawa, A.G. Yodh Thermal conductivity and interfacial resistance in single-wall carbon nanotube epoxy composites // Applied physics letters. – 2005. – V. 87. – P. 161909-161909-3.
10. W.A. DeHeer, W.S. Bacsa, A. Chatelain, T. Gerfin, R. Humphreybaker, L. Forro, D. Ugarte Aligned Carbon Nanotu be Films: Production and Optical and Electronic Properties // Science. – 1995. – V. 268. – P. 845-847.
11. J.E. Fischer, H. Dai, A. Thess, R. Lee, N.M. Hanjani, D.L. Dehaas, R.E. Smalley Metallic resistivity in crystalline ropes of single-wall carbon nanotubes // Physical Review B. – 1997. – V. 55. – P. R4921-R4924.
12. Balberg I. A comprehensive picture of the electrical phenomena in carbon black–polymer composites // Carbon. – 2002. – V. 40. – P. 139-143.
13. M. Foygel, R.D. Morris, D. Anez, S. French, V.L. Sobolev Theoretical and computational studies of carbon nanotube composites and suspensions: Electrical and thermal conductivity // Physical Review B. – 2005. – V. 71. – P. 104201-8.
14. Balberg I. Tunneling and Nonuniversal Conductivity in Composite Materials // Physical review letters. – 1987. – V. 59, №12. – P. 1305-1308.
15. Chunyu Li Dominant role of tunneling resistance in the electrical conductivity of carbon nanotube–based composites / Chunyu Li, Erik T. Thostenson, Tsu-Wei Chou // Applied physics letters. – 2007. – V. 91. – P. 22314-3.
16. Simmons J.G. Generalized Formula for the Electric Tunnel Effect between Similar Electrodes Separated by a Thin Insulating Film // Journal of Applied Physics. – 1963. – V. 34, №6. – P. 1793-1803.
17. Qianqian Li, Christian A. Rottmair, Robert F. Singer CNT reinforced light metal composites produced by melt stirring and by hight pressure die casting // Composites Science and Technology. – V. 70. – 2010. – P. 2242-2247.
18. E.V. Anufrieva, M.G.Krakovyak i dr. Vzaimodejstvie polimerov s fullerenom C_{60}// Fizika tverdogo tela.− 2002.− T. 44, V. 3. − P.443-444.
19. A.V. Eleckij, B.M. Smirnov Fullereny // Uspehi fizicheskih nauk. – 1993. − T. 163, № 2. − p. 33-60.
20. J. Keith Nelson Dielectric Polymer Nanocomposites. – Springer Science & Business Media. – 2009. – 368 p.
21. Polipropilen / Pod red. V. Pilipskogo, I. Yarceva. – M.: Himiya, 1967. – 16 p.
22. S.R. Bakshi, D. Lahiri, A. Agarwal Carbon nanotubes reinforced metal matrix composites // CRC Press, Boca Raton. – 2011. – 295 p.
23. A. Bachmaier, R. Pippan Generation of metallic nanocomposites by severe plastic deformation // International Materials Reviews. – 2013. – V. 53, №1. – P. 41-62.
24. Mikhail Nishchenko, Galina Mihajlova, G.P. Prikhodko, Tatiana Volkova, Mykola Dashevskyi, Olesya Nakonechna Peculiarities of Electrical Conductivity of Metal/Carbon Nanotubes Array // *Metallofiz. Noveishie Tekhnol.*, **40**, No. 6: 749–758 (2018),DOI: 10.15407/mfint.40.06.0749.
25. H.Yu.Mykhailova, Bogdan Kovalchuk, Yuliya Bozbey, Volodymyr Dekhtyarenko Electrical conductivity of nanocomposites metal-carbon nanotubes // MRS Communications, 13, 320-323 (2023) https://doi.org/10.1557/s43579-023-00345-2
26. *I. M. Sydorchenko, N. A. Shevchenko, Ye. A. Tsapko, I. Ye. Galstan, H. Yu. Mykhaylova, and E. G. Len* Emission Properties of Cathode Materials Based on LaNi5–CNT Composites // *Metallofiz. Noveishie Tekhnol.*, **43**, No. 12: 1707—1718 (2021) (in Ukrainian) https://doi.org/10.15407/mfint.43.12.1707
27. K.S. Novoselov, A.K. Geim, S.V. Morozov, D. Jiang, M.I. Katsnelson, I.V. Grigorieva, S.V. Dubonos, A.A. Firsov Two-dimensional gas of massless Dirac fermions in grapheme // Nature letters. – 2005. – V. 438, №10. – P. 197-200.

Al-Si-Ni composite with a low-temperature coefficient of linear expansion

Inna Kirian[1], Alexander Rud[1], Tetiana Monastyrska[1], Gennadiy Bagliuk[2], Andrey Lakhnik[1], Viktor Nosenko[1], Mykola Skoryk[1], Vitalii Bevz[1], Dmytro Pakula[1]
[1]G.V. Kurdyumov Institute for Metal Physics of N.A.S. of Ukraine, Kyiv, Ukraine
[2]I.M. Frantsevich Institute for Problems in Material Science of N.A.S. of Ukraine, Kyiv, Ukraine
kiryan.inna@gmail.com

Absract: *The melt spinning and ball-milling techniques were applied to fabricate powder Al-Si-Ni alloy. The obtained Al-Si-Ni powder was compacted in pellet and solid-state sintered at 530 °C at a pressure of ~200 MPa. The phase composition, structure, coefficient of linear thermal expansion and hardness sintered samples were determined. The coefficient of linear thermal expansion of samples formed after sintering is in the range from 14.7×10^{-6} K^{-1} to 17.5×10^{-6} K^{-1}. It is typical for steel. The synthesized powder composite, contains intermetallic Al_3Ni phase, crystalline aluminum, and silicon. The hardness of sintering samples is 113 HV.*
Keywords*: Al-Si-Ni ALLOY, COEFFICIENT OF LINEAR THERMAL EXPANSION, HOT PRESSING*

1. Introduction

The rapid development of modern industry demands new materials with unique physical, mechanical, and functional properties [1]. Close attention is paid to the evolution of technologies for obtaining new metal and metal composite materials with increased physical and chemical properties. The demand for new materials is due to several requirements. Some of them are the improvement of product characteristics, expansion of the working temperature range of materials, and protection of equipment objects from the action of destabilizing factors during operation. Aluminium-based composites with a low coefficient of linear thermal expansion (CTE), high mechanical strength, low weight, and excellent corrosion resistance are of particular interest [2, 3, 4]. It is a perspective material for the automotive, aerospace and construction industries. The materials of precision instruments for the orientation and navigation of space objects should be characterized by high resistance to micro deformation. The instability of the dimensions of the details of these materials leads to frequent errors in determining the coordinates of navigation sources. In some cases, the error can be 20-50% of the total error of the apparatus. The application of hyper eutectic alloys of the Al-Si system with a low value of CTE will avoid the above-mentioned problem. Silicon is the most important alloying element in aluminium alloys - silumins. It is introduced in large quantities in all aluminium alloys, in which the leading physical property is a low CTE value. The CTE of alloys decreases almost proportionally to the silicon concentration in the alloys. Compared with aluminium ($\alpha_{Al} \approx 22.2\times10^{-6}$ K^{-1}) silicon is characterized by a very low coefficient of thermal expansion ($\alpha_{Si} \approx 3\times10^{-6}$ K^{-1}) [5]. However, with conventional casting methods, silicon introduced into aluminium in large quantities (> 15%) forms coarse primary discharges, which strongly distort the alloy and deteriorate its mechanical and technological properties. Despite various modification methods for grinding the coarse silicon component, traditional methods cannot produce high-silicon alloys that meet all the requirements in terms of quality and material properties.

The Ni-containing high silicon content silumins are a unique group of cast aluminium alloys. The Al-Si-Ni alloys are one of the preferred materials for pistons. These alloys have high heat and wear resistance, good casting properties, high mechanical strength, and low thermal expansion [6-9]. The low CTE value ensures little volume change during piston operation and thus allows for a minimal gap between the aluminium alloy piston and the steel cylinder.

Powder metallurgy methods are widely used to obtain aluminium-based alloys with a low CTE. The high-rate solidification ensures the dispersion of all structural components, including those insoluble in the matrix of intermetallics. Several techniques have been developed in this field. The melt-spinning approach has become widely used in the production of Al-based alloys. It is characterized by a relatively higher cooling rate (10^5-10^7 K/s) during melt spinning and the ability to produce a large quantity of rapidly solidified ribbons [10]. The other technology that belongs to the category of fast solidification is the gas atomization method [11]. The cooling rate of the metal granules is generally in the order of 10^4-10^5 K/s [12]. The obtained metallic powders have spherical shapes and homogeneous structures. Next, these powders are pressed into brackets from which make with the necessary physical and mechanical properties are made.

In this paper, we introduce a method for fabricating powder of a rapidly crystallized Al-Si-Ni alloy by manufacturing a rapidly hardened metal ribbon by melt spinning followed by its dispersion in a high-energy ball mill to get a finely dispersed powder and subsequent hot pressing.

2. Materials and method

The powder Al-Si-Ni alloy was the starting material. Several methods were used to fabricate initial powders. In the first stage, the ribbons of the Al-Si-Ni alloy were produced by melt spinning technique from bulk Al-Si-Ni ingots. The chemical composition of the ribbon is Al –67 wt.%, Si – 26 wt.%, and Ni – 7 wt.%. In the second stage, the ribbons were ball milled to fabricate Al-Si-Ni powder in the second stage. The milling speed (200 rpm) and balls-to-powder mass ratio (10:1) are still the same in all experiments. The grinding time was 30 m. The obtained powder was compacted as a cylindrical pellet at a pressure of ~200 MPa. Then compressed pellet was solid-state sintered at 530 °C for 1 hour in a vacuum at a pressure of ~200 MPa. Previously sinter pellet was heated to 300 °C and held for 30 min in a vacuum to remove foreign impurities (water, hydrogen) from the surface of the powder. X-ray diffraction studies are carried out on the standard diffractometer DRON-4 with monochromatic Mo K_α-radiations in the Bragg-Brentano geometry. Rietveld refinement of the XRD patterns was performed by the MAUD software [13]. The hardness was measured by Vickers method. The microstructure study of the samples was performed on a SEM TESCAN MIRA3 microscope with EDS attachment and NEOPHOT-2 optical microscope.

3. Result and discussion

The microstructure of Al-Si-Ni alloy, which was used in the production of the fast solidification ribbon, is shown in Fig. 1a. According to the results of the metallographic analysis, it was established that the structure of the alloy is typical for hyper eutectic silumin. It can be seen that this alloy contains large silicon crystals up to 300 μm in size. According to its mechanical properties, it is very breakable. Primary Si crystals have the form of equiaxed polyhedra with different numbers of faces. Such large amounts of them lead to the brittleness of the finished products. In addition, the alloy contains other phases of eutectic origin. These phases form the triple eutectic: α-solid solution of silicon in aluminum (almost pure aluminum), silicon, and particles of Al_3Ni intermetallic. The microstructure of the powder is shown in Fig. 1b. Individual particles have an irregular shape and are characterized by a wide size distribution from 0.1 to 500 μm (Fig. 1c). The average particle size is ~ 200 μm.

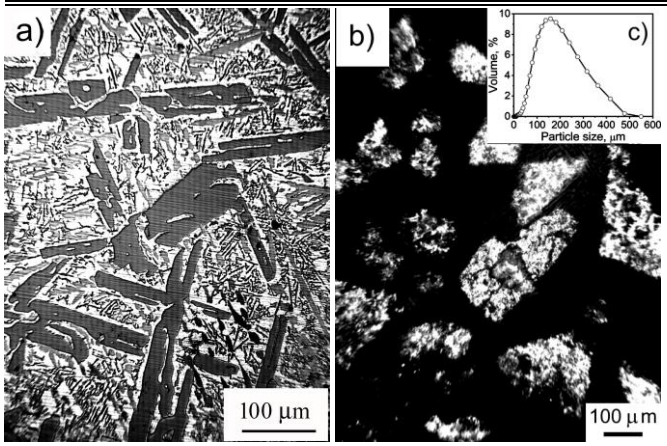


Fig. 1 *The typical microstructure of the initial Al-Si-Ni alloy – (a), powder Al-Si-Ni alloy, obtained by ball-milling of ribbon - (b) and size particle distribution - (c).*

The XRD pattern of pellet sintered from Al-Si-Ni alloy powder at 200 MPa and 530 °C following 2 hour are shown on Fig. 2. Obviously, the sample contains several phases. The best Rietveld refinement for the sintered sample was obtained for the three phases: fcc - Al, fcc typical for diamond - Si, and orthorhombic - Al_3Ni. The reflex from the initial Ni is absent in the XRD pattern.

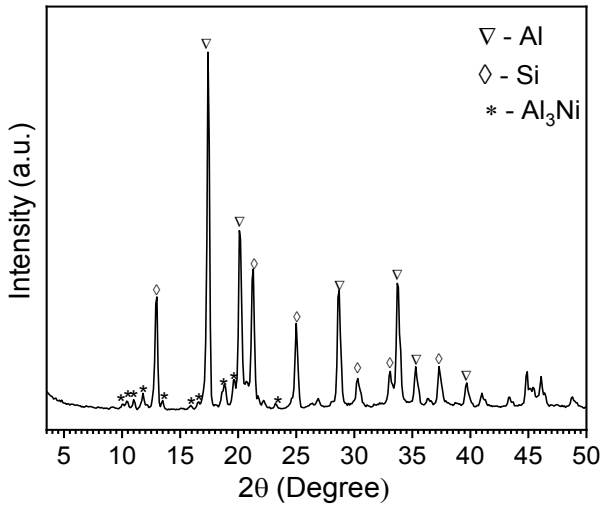


Fig. 2 *XRD pattern of a solid phase sintering composite.*

The phase composition and structural parameters of the composite are represented in Table 1.

Table 1: *The phase composition and structural parameters of the composite.*

Phase	Lattice parameters (Å)			Crystalline size (Å)	Abundance (wt.%)
	a	*b*	*c*		
Al	4.0489	–	–	800	63
Si	5.4289	–	–	1180	24
Al_3Ni	6.5770	7.3544	4.8151	660	13

The percentage of the Al, Si, and Al_3Ni phases in the sample was estimated by full-profile analysis is about ~63, ~24, and ~13 wt.%, respectively. The domain sizes are 800 Å, 1080 Å, and 660 Å for Al, Si, and Al_3Ni, respectively. The lattice parameter calculated from these peaks for Al is a = 4.0489 Å, and for Si is a = 5.4289 Å. The lattice parameters calculated for the Al_3Ni phase are a = 6.5770 Å, b = 7.3544 Å, and c = 4.8151 Å.

The typical microstructure of sintered composite from powder Al-Si-Ni alloy is shown in Fig. 3. Composite differs in structure from the initial alloy (see Fig. 1a). Silicon crystals are evenly distributed over the entire sample volume. Such a structure will contribute to obtaining a material with increased physical and mechanical properties.

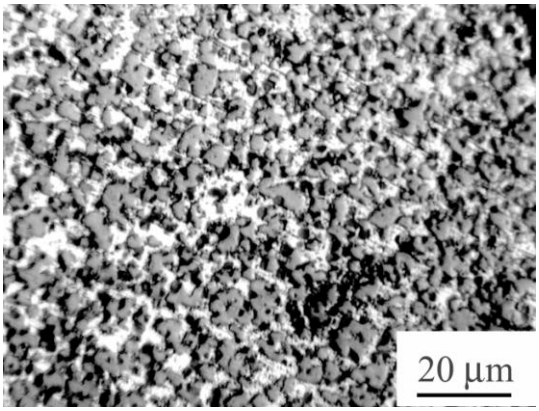


Fig. 3 *Typical microstructure of sintered composite.*

One of the essential characteristics of Al-Si-Ni alloys is a low coefficient of linear thermal expansion. These alloys are widely used in precision instruments. A negligible deviation in the size of parts can lead to undesirable consequences. The value for Al-Si-Ni alloys must be in diapason from 14.5×10^{-6} K^{-1} to 17×10^{-6} K^{-1}. This CTE value is close to typical for steel. The CTE measurement of the sintered Al-Si-Ni alloy sample was performed on a dilatometer equipped with an induction linear transducer to measure linear sample elongation. The specimen was placed into the chamber, and its vacuum was carried out. After that, the chamber was filled with helium and heated from room temperature to 200 °C. A typical change in sample size is shown in Fig. 4. It can be seen that the thermal expansion of the sample occurs according to a linear law.

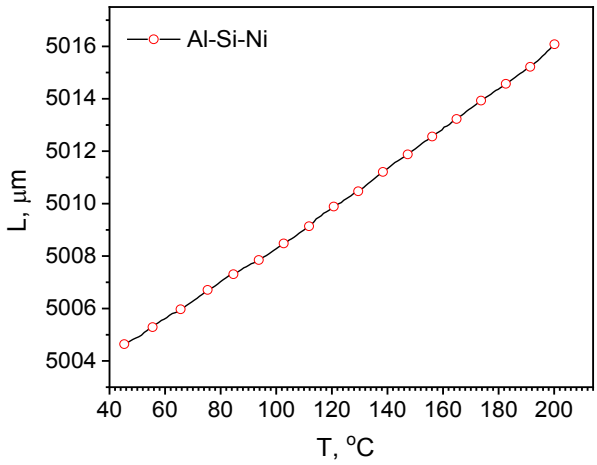


Fig. 4 *The curves of temperature dependence size change of sintered composites.*

The coefficient of linear thermal expansion in dependence on temperature was calculated based on the experimental data accordingly to the following equation:

$$\alpha = \frac{1}{l_0}\frac{l_{i+1}-l_i}{T_{i+1}-T_i}$$

where α – the coefficient of linear thermal expansion; l_0 – the initial length of the sample; T_i – is the initial temperature of the *i-th* interval; T_{i+1} is the final temperature of the *i-th* interval; l_{i+1}–l_i – sample length change in the *i-th* temperature interval. The calculated data are represented in Table 2. It can be seen that the CTE of the sintered sample, depending on the temperature, is in the

range from 14.7×10^{-6} K^{-1} to 17.5×10^{-6} K^{-1}. The obtained values correspond to the standards required for Al-Si-Ni alloys.

Vickers hardness values measured on the sintered samples also is presented in Table 2. The hardness obtained for sintered compact is 113 HV.

Table 2: *The coefficient of linear thermal expansion, and hardness of sample.*

Sample	CTE, 10^{-6} K^{-1}				HV
	50 °C	100 °C	150 °C	200 °C	
Al-Si-Ni	14.7	14.9	16.2	17.5	113

The EDS mapping of elements was carried out to get the elemental distribution in the sintered samples t. Fig. 5 shows the SEM image and elements distribution map. At the same time, we can see the non-uniform distribution for aluminium and silicon. Also, we can observe the high aluminium concentration areas like bright spots (see Fig. 5b) on the EDS maps. In addition, dark spots on the EDS maps of aluminium (Fig. 5b) and silicon (Fig. 5c) are present. These dark spots mean lower concentrations of aluminium and silicon in these areas. It is meaningful the bright spots on the aluminium EDS map (Fig. 5b) and the dark spots on the silicon EDS map (Fig. 5c) are overlapped. So, when we superimpose the EDS mapping results with the SEM image, we may most probably attribute the dark grey spots (Fig. 5a) to the silicon particle. In addition, it is visible that the nickel is almost and is uniformly distributed over the cross-section of the sample (Fig. 5d). However, bright spots are observed on the nickel EDS map overlap with less bright spots on the aluminium EDS map (Fig. 5b). According to the results of the XRD analysis, it was established that the sintered sample contains three phases: Al, Si, and Al_3Ni. Based on this, the light spots on the SEM image can be attributed to the Al_3Ni phase (Fig. 5a).

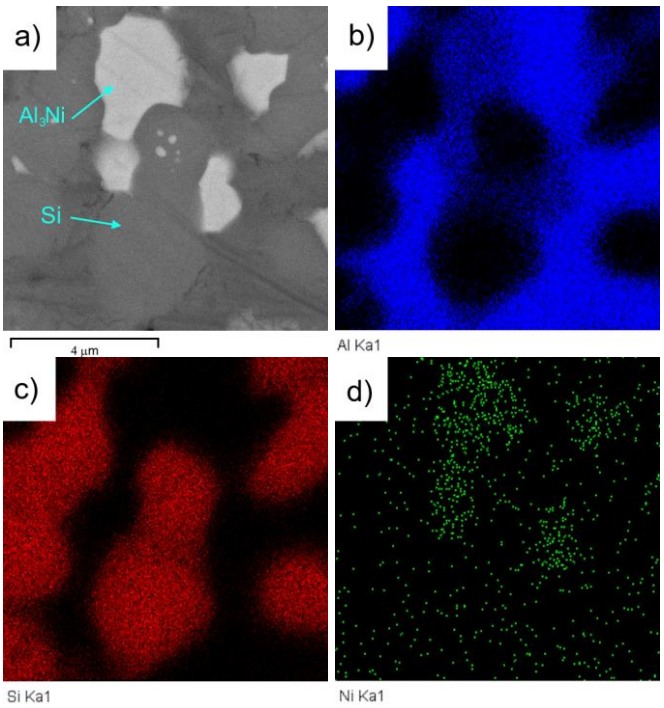


Fig. 5 *Typical micrographs of composite – (a) and element distribution maps: Al – (b), Si – (c), Ni – (d).*

4. *Conclusion*

Bulk composite material from powder Al-Si-Ni alloy is successfully fabricated by sintered at pressure. It has been found the proposed technique allows for obtaining samples with a homogeneous structure. The CTE measurements for the sintered sample suggest the value is within the range of 14.7×10^{-6} K^{-1} to 17.5×10^{-6} K^{-1} and meets technological standards Al-Si-Ni alloy. The hardness of sintered pellet is 113 HV.

Acknowledgments

The work is being carried out within the framework of competitive research programs of the National Academy of Sciences of Ukraine.

5. References

1. P.K. Dinesh Kumar, S. Darius Gnanaraj, *Eng. Res. Express. 5*, 022002 (2023)
2. V. Vijayan, M. Ravi, K. Narayan Prabhu, *Mater. Today: Proc.* 46 (7), 2732 (2021)
3. V.I. Razumovskiy, Yu.Kh. Vekilov, I.M. Razumovskii, A.V. Ruban, V.N. Butrim, V.N. Mironenko, *Phys. Solid State.* 53, 2189 (2011).
4. X. Dong, L. He, P. Li, *J. Alloys Compd.* 612, 20 (2014)
5. B. Kucharska, J. Kowalczyk, *Acta Phys. Pol. A.* 129, 197 (2016)
6. R. Kakitani, C.B. Cruz, T.S. Lima, C. Brito, A. Garcia, N. Cheung, Materialia, 7, 100358 (2019)
7. G. Liang, Y. Ali, G. You, M.-X. Zhang, *Materialia*, 3, 113 (2018)
8. Y. Li, Y. Yang, Y. Wu, L. Wang, X. Liu, *Mater. Sci. Eng. A.* 527, 7132 (2010)
9. M. Zeren, *Mater. Des.* 28, 2511 (2007)
10. Y. Lin, B. Wu, S. Li, S. Mao, X. Liu, Y. Zhang, L. Wang, *Mater. Sci. Eng.* 621, 212 (2015).
11. D. Tourret, G. Reinhart, C.-A. Gandin, G.N. Iles, U. Dahlborg, M. Calvo-Dahlborg, C.M. Bao, *Acta Mater.* 59, 6658 (2011)
12. T. Bedo, B. Varga, D. Cristea, A. Nitoi, A. Gatto, E. Bassoli, G. Bulai, I.-L. Velicu, I. Ghiuta, S. Munteanu, M. Alin Pop, C. Gabor, M. Cosnita, L. Parv, D. Munteanu, *Metals*. 9(5), 483 (2019)
13. Lutterotti MAUD: Material Analysis Using Diffraction (http://maud.radiographema.eu/)

Long-time phase transitions in various vegetable oils

Leszek T. Pawlicki
Warsaw University of Technology, Faculty of Physics, Warszawa Poland,
leszek.pawlicki@pw.edu.pl

Abstract: *Vegetable oils are mixtures of mainly triglycerides of fatty acids. Their particles are large and have significantly different shapes. This causes problems in matching the molecules to each other and their translation and rotation necessary for the phase transition to occur. All this causes that phase transformations in vegetable oils have a long-time character. This article presents a comparison of the times of occurrence of this type of pressure-induced transformations for olive, sunflower, rapeseed and other oils. Possible causes of differences between them were also analyzed. The analysis of the phenomena occurring during phase transformations is crucial because during them the mechanical and electrical properties of oils change rapidly.*
KEY WORDS: *HIGH PRESSURE, TRIGLICERIDES, VEGETABLE OILS, PHASE TRANSITIONS*

1. Introduction

Vegetable oils are a very important source of energy for humans. They are also a source of many omega fatty acids (including Omega-3) which have a key, beneficial effect on the functioning of many living organisms (including humans) [1-4]. For this reason, these oils are used in many industries: food, pharmaceutical, medical, etc. It is therefore important to know the properties of these oils, e.g. physical ones. These properties strongly change during phase transitions. Hence, this article is devoted to these transformations obtained by the compression.

Pressure-induced phase transitions occurring in vegetable oils and their constituents have been studied for a long time. The main components of vegetable oils are triglycerides. Both in the case of triglycerides and vegetable oils composed of them, the studies conducted on the phase transitions taking place in them have shown their long-time nature. Such transformations may take place from a few hours to several days. Under unfavorable conditions, such transformations may not even occur at all [5-39]. In this work, I will discuss the main factors causing such a slow rate of pressure-induced phase transitions in vegetable oils.

2. Results of discussion

2.1 Influence of the structure of triglyceride molecules on the rate of phase transitions

Phase transitions require translations and rotations of molecules to match each other. Vegetable oils are mixtures of triglycerides of fatty acids (with a small addition of other substances). Their large particle size makes it difficult for them to move and rotate inside the oil. This significantly extends the phase transition even in comparison to phase transitions occurring for free fatty acids whose acid residues are elements of triglyceride molecules. The presence of three arms formed from chains of fatty acid residues additionally complicates the mutual movement of molecules [5-39].

The molecules of the already mentioned triglycerides consist of a glycerin molecule with three chains of acid residues connected to it, forming three arms. These arms can have different shapes and be arranged at different angles to each other. There are three crystal forms in triglycerides and their mixtures (oils): alpha, triple and double. The transition between successive forms requires changing the shapes of the particles from fork to chair form (requires deformation of particles). This causes a significant slowdown of phase transformations occurring in oils [6-10].

Saturated fats, such as butter, are mainly composed of triglycerides of saturated acids. This means that the fatty acid residues present in their molecules have only single bonds between carbon atoms. This makes their arms straight. Vegetable oils consist mainly of triglycerides of unsaturated fatty acids. This means that there are double bonds between the carbon atoms in their chains of acid residues. This in turn results in the bending of these chains and the formation of shapes resembling hooks. This causes the molecules of these triglycerides to tangle with each other. They are also harder to match. This is one of the reasons why saturated fats solidify at a higher temperature than vegetable oils [5-39].

Among the unsaturated fatty acids there are not only those with one double bond, such as oleic acid, but also with more bonds, for example linoleic acid (two bonds). For this reason, the chain of the linoleic acid molecule is bent more strongly than for oleic acid. This causes oils containing mainly triglycerides of linoleic acid, such as sunflower oil, to undergo phase changes much more slowly than those containing mainly triglycerides of oleic acid, such as olive oil [34-39].

The complex triglyceride molecules of various unsaturated fatty acids have different shapes. This makes it much more difficult to fit such different molecules into shape inside the vegetable oil. As a result, oils that are mixtures of different triglycerides generally undergo phase changes much slower than pure triglycerides [11-39].

Since phase transformations in vegetable oils are of a long-time nature, it is not enough to reach the appropriate threshold pressure for their occurrence, but often it is also necessary to wait an appropriate period of time to reach them [11-39].

2.2 Influence of oil compression speed on phase change rate

The speed of their compression has a significant impact on the rate of pressure-induced phase transitions in vegetable oils. Due to the aforementioned hooks present in the chains of unsaturated acid residues present in the molecules of their triglycerides, these molecules can be strongly entangled. Such entanglement causes that above a certain limiting rate of compression, the rate of phase changes decreases with increasing compression rate. Above a certain compression rate, entanglement completely blocks the transfer and rotation of molecules, and phase transitions do not occur in inches. The oil then behaves like a typical non-Newtonian fluid, becoming very hard but still liquid [27-39].

3. Summary and conclusions

In the case of vegetable oils, phase transitions are long-time. The basic internal factors influencing the rate of phase transformations in a given oils are the size and complicated structure of its molecules, the presence and number of multiple bonds in the chains of acid residues, the need to change the shape of the molecule during transformation and the multitude of shapes of molecules of various triglycerides included in the oil. The main external factor influencing the rate of phase transitions induced in vegetable oils is the rate of oil compression [11-39].

4. References

[1] R.W. Owen, A. Giacosa, W.E. Hull, R. Haubner, G. W¨urtele, B. Spiegelhalder, and H. Bartsch. Olive-oil consumption and health: The Possible Role of Antioxidants. Lancet Oncology, 1(2):107–112, (2000).

[2] D. Boskou, M. L. Clodoveo, Olive Oil: Processing Characterization, and Health Benefits, Foods 9(11) 1612, (2020).

[3] A. Foscolou, E. Critselis, S. Tyrovolas, Ch. Chrysohoou, L. S. Sidossis, N. Naumovski, A. L. Matalas, L. Rallidis, E. Polychronopoulos, J. L. Ayuso-Mateos, J. M. Haro and D. Panagiotakos, The Effect of Exclusive Olive Oil Consumption

on Successful Aging: A Combined Analysis of the ATTICA and MEDIS Epidemiological Studies, Foods 8(1), 25 (2019).
[4] E. M. Yubero-Serrano, J. Lopez-Moreno, F. Gomez-Delgado, J. Lopez-Miranda, Extra Virgin Olive Oil: More Than a Healthy Fat, Europian Journal of Clinical Nutrition 72, 8-17 (2019).
[5] R. M. Siegoczyński, J. Jędrzejewski and R. Wiśniewski, Long Time Relaxation Effect of Liquid Castor Oil Under High Pressure Condition, High Pressure Research. 1, 225 – 301 (1989).
[6] R. H. Ferguson and E. S. Lutton, The Polymorphism of Triolein, Journal of the American Chemical Society 69(6), pp. 1445–1448 (1947).
[7] Ch. Akita, T. Kawaguchi and F. Kaneko, Structural Study on Polymorphism of Cis-Unsaturated Triacylglycerol: Triolein, The Journal of Physical Chemistry B 110 p. 4346-4353 (2006).
[8] F. F. Hollander, S. X. M. Boerrigter, J. van de Streek, P. Bennema, H. Meekes, J. Yano and K. Sato, Comparing the Morphology of β-n.n.n. with β'-n.n+2.n and β'-n.n.n-2 Triacylglycerol Crystals, The Journal of Physical Chemistry B 107 p. 5680-5689 (2003).
[9] K. Sato, Solidification and Phase Transformation Behaviour of Food Fats – a review, Fett/Lipid 101(12), pp. 467–474 (1999).
[10] K. Sato, Crystallization Behaviour of Fats and Lipids – a review, Chemical Engineering Science 56 p. 2255-2265 (2001).
[11] A. J. Rostocki, D. B. Tefelski , S. Ptasznik, Compressibility Studies of Some Vegetable Oils up to 1 GPa, High Pressure Research, Volume 29, Issue 4, Pages 721-725 (2009).
[12] A. J. Rostocki, D. B. Tefelski and K. Wieja, The Equation of State of Triolein up to 1 GPa, High Pressure Research 31 p. 168-171 (2011).
[13] P. Ferstl, S. Gillig, C. Kaufmann, C. Dürr, C. Eder, A. Wierschem, and W. Ruß, Pressure Induced Phase Transitions in Triacylglycerids, Annals of the New York Academy of Science 1189, pp. 62–67 (2010).
[14] P. Ferstl, C. Eder, W. Ruß and A. Wierschem Pressure-induced Crystallization of Triacylglycerides, High Pressure Research Vol. 31, No. 2, 339–349 (2011).
[15] R. M. Siegoczyński, J. Jędrzejewski, R. Wiśniewski; The Influence of Pressure on the Refractive Index of Castor Oil up to 0.8 GPa., High Pressure Research, 8, 439-441 (1991).
[16] R. Wiśniewski, J. Jędrzejewski, R. M. Siegoczyński, A. Tkacz, Volume Changes of Castor Oil During its Transformation to the High Pressure Phase, High Pressure Research, 11, 385 –391 (1994).
[17] R. Wiśniewski, J. Jędrzejewski, R. M. Siegoczyński, Dielectric Permittivity and Dielectric Loss of Castor Oil During its Transformation to the High Pressure Phase, High Pressure Research., 13, 41 – 45 (1994).
[18] R. Wiśniewski, R. M. Siegoczyński, A. J. Rostocki, Viscosity Measurement of Some Castor Oil Based Mixtures Under High Pressure Conditions , High Pressure Research, 25, 63-70, (2005).
[19] R.M. Siegoczyński, R. Wiśniewski, and W. Ejchart. On the Structure of a Pressure-induced New Phase in Castor Oil. Journal of Molecular Liquids, 107(1-3):257–261, (2003).
[20] R. M Siegoczyński, A.J. Rostocki, P Kiełczyński and M. Szalewski, A Viscosity Measurement During the High Pressure Phase Transition in Triolein, Journal of Physics: Conference Series 121 142010 (2008).
[21] A. J. Rostocki, R. M. Siegoczyński, P. Kieczyński, M. Szalewski, An Application of Love SH Waves for the Viscosity Measurement of Triglycerides at High Pressures, High Pressure Research, Volume 30, Issue 1, Pages 88-92 (2010).
[22] D. B. Tefelski, C. Jastrzębski, M. Wierzbicki, R. M. Siegoczyński, A. J. Rostocki, K. Wieja & R. Kościesza, Raman Spectroscopy of Triolein Under High Pressures, High Pressure Research v. 30, p. 124-129 (2010).
[23] A. Kos, D. B. Tefelski, R. Kościesza, A. J. Rostocki, A. Roszkiewicz, W. Ejchart, C. Jastrzębski and R. M. Siegoczyński, Certain Physico-chemical Properties of Triolein and Methyl Alcohol-triolein Mixture Under Pressure, High Pressure Research 27 p. 39-42 (2007).
[24] D. B. Tefelski, A. J. Rostocki, A. Kos, R. Kościesza and R. M. Siegoczyński, Pressure Induced Volume Changes in Triolein with Addition of Methyl Alcohol, High Pressure Research 27 p. 57-61 (2007).
[25] R. Wiśniewski, R.M. Siegoczyński, A. Długosz, M. Przewłocki, M. Szymański, and M. Trzeciecki. Investigations of Triolein Under High Pressure. High Temperatures - High Pressures, 33(2):231–236, (2001).
[26] A. Roßbach, L. A. Bahr, S. Gäbel1, Andreas S. Braeuer, A. Wierschem, Growth Rate of Pressure-induced Triolein Crystals, Journal of the American Oil Chemists' Society, v. 96 pp. 25-33 (2019).
[27] A. J. Rostocki, R. Wiśniewski, T. Wilczyńska, High Pressure Phase Transition in Rape-seed Oil, Journal of Molecular Liquids 135 (2007) p. 120-122.
[28] R. Kościesza, A. J. Rostocki, A. Kos, D. B. Tefelski, R. M. Siegoczyński and Ł. Zych, Observation of Pressure-induced Phase Transitions in Rapeseed Oil with Methyl Alcohol Mixtures, High Pressure Research 27 (2007) p. 51-55.
[29] A. J. Rostocki, R. Kościesza, D. B. Tefelski, A. Kos, R. M. Siegoczyński and Ł. Chruściński, Pressure-induced Phase Transition in Soy Oil, High Pressure Research 27 (2007) p. 43-46.
[30] Á. Guinda, M. C Dobarganes, M. V. Ruiz-Mendez, M. Mancha, Chemical and Physical Properties of a Sunflower Oil with High Levels of Oleic and Palmitic Acids, European Journal Lipid Science Technology 105, 130–137, (2003).
[31] R. Tarakowski, A. Malanowski, R. Kościesza, R. M. Siegoczyński, VIS Spectroscopy and Pressure Induced Phase Transitions – Chasing the Olive Oils Quality, Journal of Food Engineering 122 (2014) p. 28-32.
[32] A. J. Rostocki, R. Tarakowski, P. Kiełczyński, M. Szalewski, A. Balcerzak, S. Ptasznik, The Ultrasonic Investigation of Phase Transition in Olive of Oil up to 0.7 GPa, Journal of the American Oil Chemists Society 90 (2013) p. 813-818.
[33] B. Guignon, C. Aparicio and P. D. Sanz, Volumetric Properties of Sunflower and Olive Oils at Temperatures Between 15 and 55 ˚ C Under Pressures up to 350 MPa, High Pressure Research 29 (2009) p. 38-45.
[34] L. T. Pawlicki, R. M. Siegoczyński, S. Ptasznik, K. Marszałek, Compressibility Studies of Olive Oil, Journal of Biotechnology and Biomedicine 4, 187-195 (2021).
[35] L. T. Pawlicki, M. K. Urbański, D. Tefelski, R. M. Siegoczyński, Viscosity Measurement of Olive Oil Under Pressure, Food Science & Nutrition Technology 6 issue 5 (2021).
[36] L. T. Pawlicki, R. M. Siegoczyński, S. Ptasznik, K. Marszałek, Electric Properties of Olive Oil Under Pressure, European Food Research and Technology, 247(8), 1933-1937 (2021).
[37] L. T. Pawlicki, A. J. Rostocki, D. B. Tefelski, R. M. Siegoczyński and S. Ptasznik, Mechanical Properties of Sunflower Oil Under Pressure, European Food Research and Technology 248 p. 283-287 , (2022).
[38] L. T. Pawlicki, A. J. Rostocki, D. B. Tefelski, R. M. Siegoczyński and S. Ptasznik, Electric Properties of Sunflower Oil Under Pressure, International Journal of Scientific Engineering and Applied Science v. 8, issue, 214-227 (2022).
[39] L. T. Pawlicki, Pressure-induced Long-time Phase Transitions in Selected Choosen Vegetable Oils, Materials Science. Non-Equilibrium Phase Transformations." Vol. 8, Issue 1 (2022).

Mechanical and microstructure features of ti-al damping materials

[*]Denys V. Oryshych, Oleksandr O. Stasiuk, Dmytro V. Pakula, Vasyl I. Nevmerzhytskyi, Vasyl P. Tkachuk
[*]G. V. Kurdyumov Institute for Metal Physics of the N.A.S. of Ukraine - Kyiv, Ukraine
[*]E-mail: den.oryshych@gmail.com

Abstract: *Currently, metallic materials featuring a porous structure are extensively employed in passive safety mechanisms for absorbing mechanical energy during dynamic loads. Among these, aluminum foam-based damping materials are the most prevalent due to their adequate processability and cost-effectiveness. Nonetheless, expanding the array of properties within damping materials necessitates exploring the utilization of porous titanium-based products, known for possessing exceptional specific strength metrics. This avenue emerges as one of the most promising ways for advancing the domain of damping and energy-absorbing materials.*
KEYWORDS: *DAMPING PROPERTIES TITANIUM ALLOYS, POWDER METALLURGY, DAMPING CAPACITY.*

1. Introduction

Presently, materials possessing a remarkable capacity to dissipate elastic strain energy during mechanical vibrations or wave propagation find widespread application in vibration suppression. This category of materials is commonly referred to as damping materials. Creating porous materials stands as an effective approach to achieve elevated damping rates. Notably, porous materials like aluminum and titanium exhibit an array of distinctive physical attributes: low thermal conductivity, heightened specific stiffness, gas permeability, and remarkable impact energy absorption [1–3]. The advantageous feature of these materials is their low density, rendering them suitable for producing lightweight structural components intended for utilization in automotive deformation zones [2].

In a broader context, titanium and its alloys demonstrate superior specific strength compared to aluminum alloys, presenting porous titanium and its alloys [4] as potential contenders for substantially enhancing the crash energy absorption characteristics in the frontal regions of high-speed transportation systems. Diverse methodologies have been proposed for obtaining porous titanium [4], encompassing techniques like powder compaction (suspension sintering), reactive sintering, sintering of hollow spheres [4], and gas entrapment methods. Nonetheless, these manufacturing approaches might impose limitations on the material's porosity.

Notably, recent advancements have showcased the feasibility of open-cellular, porous Ti-Al intermetallic alloys synthesized through a combustion reaction involving titanium and aluminum powders [5].

2. Materials and methods

The material underwent synthesis utilizing powder metallurgy techniques employing a hydride-based approach. Commencing with titanium hydride and aluminum PA powders as initial constituents, powders of predetermined dimensions were blended and compacted. Subsequently, the resulting compacts were subjected to sintering within a residual vacuum of 10^{-3} Pa, with a heating rate of 7 °C/min, progressing to a temperature of 1250 °C. During this progression, hydrogen was entirely eliminated from the material. Subsequent to this, an isothermal annealing process was carried out at this temperature for approximately 2 hours. Following the isothermal annealing procedure, the material was subjected to cooling within a vacuum environment alongside the furnace.

X-ray investigations for determining the phase composition of powders and composite materials were conducted using the RIGAKU ULTIMA-3M diffractometer. CuKα1,2 radiation (λCuKα1 = 0.154187 nm) and a graphite monochromator were employed in the X-ray diffraction studies, following the "θ-2θ" methodology (detector step increment of 0.02°). Diffraction patterns were processed using the RIR and Rietveld analysis software packages.

The microstructure of the material, volumetric fraction, morphology of residual pores, as well as their uniform distribution throughout the composite volume, were investigated by using optical microscopy (Olympus IX-70) and scanning electron microscopy (TESCAN VEGA 3). Metallographic samples were prepared through mechanical grinding, followed by polishing using Al2O3 suspension with Struers LaboPol-21 and LECO Spectrum System 1000 equipment.

3. Results and discussion

Figure 1 shows the microstructure of materials with 20% aluminum. The microstructure is characterized by relatively uniform homogeneity. Inside the pores, a "loose" structure of intermetallic compounds can be observed.

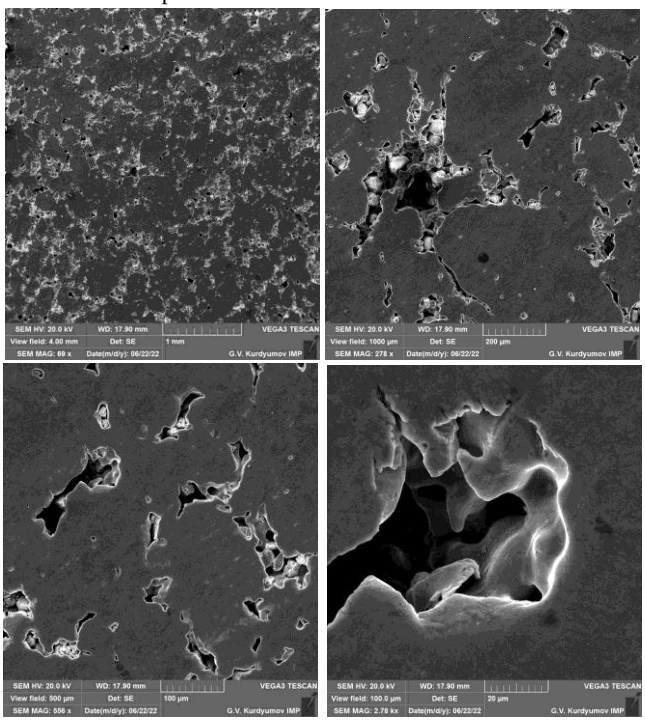


Fig. 1. *As-sintered material with 20% aluminum.*

The microstructure of the obtained intermetallic (Ti-30Al), shown in Fig. 2 has a similar appearance. A higher porosity is observed in comparison to the Ti-20%Al material (Figure 1). Inside the pores, the structure of the material also looks “loose” due to the formation of intermetallics. This structural effect cannot be removed at this sintering temperature, as the melting temperature of the intermetallic is significantly higher.

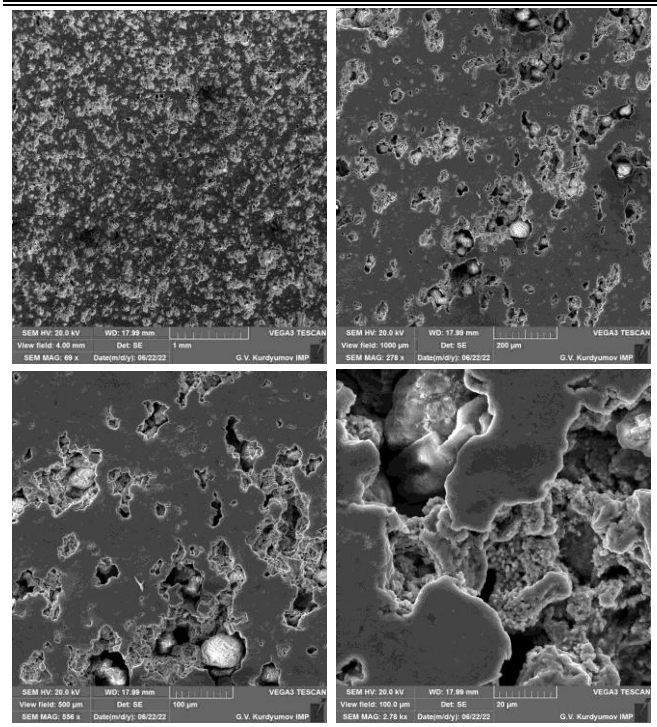


Fig. 2. *As-sintered material with 30% aluminum.*

Results. X-ray phase analysis reveals the presence of two phases, TiAl and Ti3Al, in the material (Figure 3). The TiAl phase has a tetragonal lattice, while the Ti3Al phase has a hexagonal lattice. However, upon detailed analysis of the obtained results, it can be noticed that some diffraction angles of these phases have the same values. For the composition Ti-20Al, the phase ratio was 30TiAl-70Ti3Al. For the composition Ti-30Al, the ratio between the γ phase TiAl and the α2 phase Ti3Al is equal.

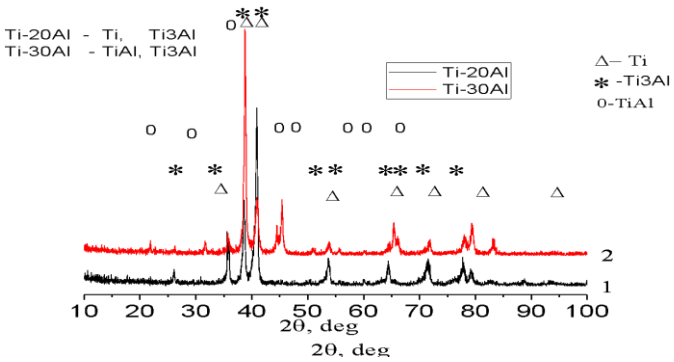


Fig. 3. *The X-ray diffraction patterns of Ti-Al system materials.*

Stress-strain curves of the tested Ti-20Al materials, compressed within a quasi-static range, are illustrated in Figure 4. Compression tests were conducted at two deformation rates: the standard rate according to ASTM standards ($\varepsilon=10^{-1}$ s^{-1}) and a faster rate ($\varepsilon=10^{-3}$ s^{-1}). These materials demonstrate plastic deformation quantitatively equal to 10%. Mechanical properties of the material slightly increase with higher deformation rates. For instance, strength rises from 250 MPa to 315 MPa, along with an increase in deformation.. It is worth noting that sample failure occurs at a 45-degree angle, aligning with fracture theory (Fig. 4 b).

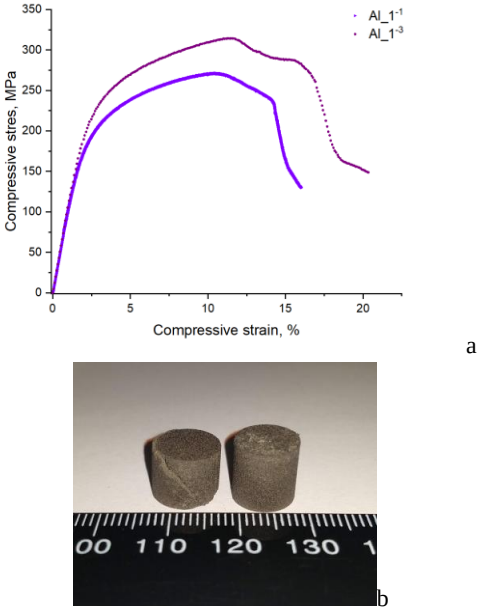


Fig. 4. *Load curves of intermetallic Ti-20Al and appearance of samples before and after deformation.*

Stress-strain curves of the tested Ti-30Al-based materials, compressed within a quasi-static range, are depicted in Fig. 5. Compression tests were carried out for the Ti-30Al intermetallic, similar to Ti-20Al, at two deformation rates: the standard rate according to ASTM standards ($\varepsilon=10^{-1}$ s^{-1}) and a faster rate ($\varepsilon=10^{-3}$ s^{-1}).

With an increased rate, the material exhibits slightly enhancement in mechanical properties. For instance, strength increases from 100 MPa to 130 MPa, along with an increase in deformation. It is noteworthy that sample failure occurs at a 45-degree angle, aligning with fracture theory.

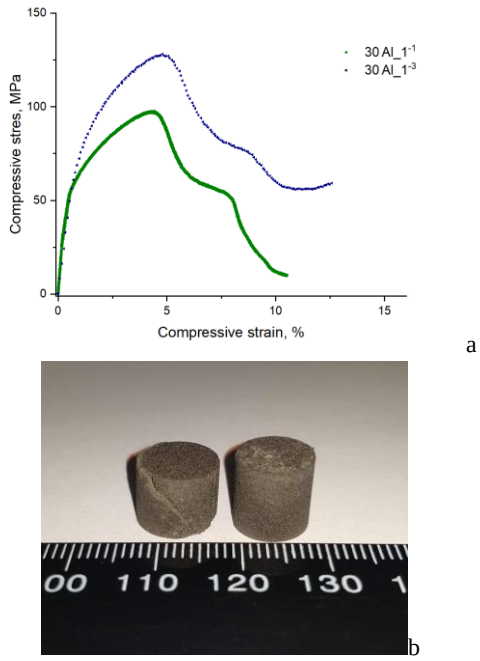


Fig. 5. *Load curves of intermetallic Ti-30Al and appearance of samples before and after deformation.*

The difference between these two systems can be explained by their distinct phase compositions. The α2-Ti_3Al phase is more brittle than the γ-TiAl phase due to the higher solubility of intermediate impurities within the α2-Ti_3Al phase. The γ-TiAl

phase acts as a "gas absorber," enhancing its ability to deform plastically even at low temperatures. Additionally, the tetragonal γ-TiAl phase diminishes as the aluminum content decreases, which positively affects dislocation mobility and consequently lowers low-temperature plasticity. Furthermore, certain γ-TiAl and α2-Ti_3Al alloys also contain additional β/β2 phases in the form of particles, formed by the introduction of chromium, molybdenum, and tungsten. The plasticity and strength of γ-alloys are governed by their chemical composition and microstructure. Low-temperature plasticity is the primary hurdle for practical utilization of γ-TiAl alloys based on Ti. Therefore, an increase in the aluminum content contributes to enhancing mechanical properties.

The damping ability of Ti-20Al material is presented in Fig. 6 as an amplitude-time dependency with the Resonance Frequency Damping Analyzer (RFDA) results. The represented damping amplitude is for the material synthesized from hydride powders and aluminum powder, resulting in a final porosity of 30%. Another plot illustrates the determination of the resonance frequency for this material along with its amplitude. Unlike pure titanium, this material exhibits two distinct resonance frequencies around 5000 and 14000 Hz.

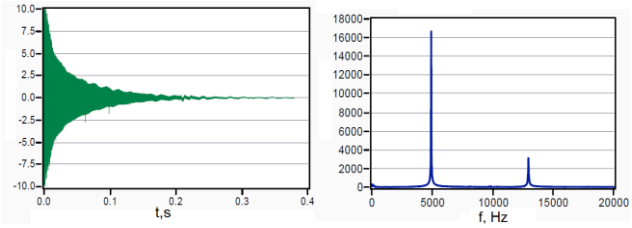


Fig. 6. *Damping properties of intermetallic Ti-20%Al*

The damping ability of Ti-30Al material is illustrated in Figure 7 through an amplitude-time dependency with the Resonance Frequency Damping Analyzer (RFDA) outcomes. The presented damping amplitude is for the material synthesized from hydride powders and aluminum powder, resulting in a final porosity of 40%. Another graph outlines the determination of the resonance frequency for this material and its amplitude. Unlike pure titanium, this material displays two distinct resonance frequencies around 4500 and 11500 Hz.

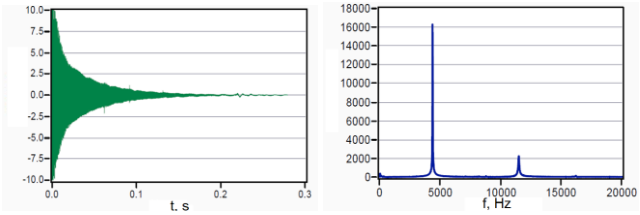


Fig. 7. *Damping properties of intermetallic Ti-30%Al*

The time required for each material to cease vibration is a qualitative indicator of its damping capability. For intermetallic materials obtained by this method, the decay time differs slightly. For Ti-20Al, it takes 0.38 seconds for vibrations to cease, while for the Ti-30Al intermetallic, this time decreases to 0.28 seconds. However, the damping coefficients differ by 0.7 (1.7 for Ti-30Al and 1 for Ti-20Al). Ti-30Al demonstrates better damping performance, which can be attributed to its slightly higher porosity and the presence of two phases in the material (i.e., interphase transitions additionally absorb energy). It is also worth noting that the damping curve for Ti-30Al is smoother than for Ti-20Al, which, in the region of active decay, resembles a sinusoid with fluctuations in amplitude, providing a significant contribution to the overall damping capability of the material.

4. Conclusions

Porous Ti-Al alloys were synthesized with different proportions of TiH2 and Al powder mixtures. There is two phases in material with 20% aluminum: Ti_3Al and pure titanium. The residual porosity of this material is 30%. In the material synthesized with 30% Al, two phases were present: γ-TiAl and α2-Ti_3Al. The residual porosity was 40%. It was demonstrated that these alloys exhibit a high energy absorption capacity (damping time of elastic waves is 0.3-0.4 seconds, and damping coefficient ranges from 1 to 1.7) due to their porous structure.

5. References

1. John Banhart. Manufacture, characterisation and application of cellular metals and metal foams. Progress in Materials Science. V. 46, Issue 6, 2001. https://doi.org/10.1016/S0079-6425(00)00002-5
2. P. Lefebvre, J. Banhart, D. C. Dunand. Porous Metals and Metallic Foams: Current Status and Recent Developments. Advanced Engineering Materials. 2008. https://doi.org/10.1002/adem.200800241
3. John Banhart. Light-Metal Foams—History of Innovation and Technological Challenges. Advanced Engineering Materials. 2012. https://doi.org/10.1002/adem.201200217
4. D.C. Dunand. Processing of titanium foams. Advanced engineering materials, 2004. https://doi.org/10.1002/adem.200405576
5. Q. Xu, B. Gabbitas, S. Matthews, D. L. Zhang. The Effect of Binder and Plasticizer on Porous Titanium Compacts Prepared by Slip Casting. Procedia Materials Science, Volume 4, 2014 https://doi.org/10.1016/j.mspro.2014.07.601.

Effects of magnetohydrodynamic treatment and alloying on the structure and properties of Al-Si-Mg casting alloys

Tetiana Monastyrska[1], Alla Berezina[1], Oleh Molebny[1], Vladyslav Fikssen[2]
[1]G.V. Kurdyumov Institute for Metal Physics of the NAS of Ukraine, Kyiv, Ukraine
[2]Physico-Technical Institute of Metals and Alloys of the NAS of Ukraine, Kyiv, Ukraine
E-mail: monast@imp.kiev.ua, beres@imp.kiev.ua, moleb@imp.kiev.ua, vfixsen@i.kiev.ua

Absract:*The possibility of improving the structure and properties of aluminum cast alloy based on Al-Si-Mg due to the melt treatment in the magnetohydrodynamic installation has been studied in this work. Also, the optimization of the chemical composition and select the optimal modes of heat treatment of the alloys to improve the structure and complex of properties was carried out. It was shown that the most effective alloying element which improve the strength characteristics of Al-Si-Mg alloy is lithium. It was found that the introduction of lithium into the alloy in the amount of 0.2% leads to the modification of the Al-Si eutectic and provides the increase in the yield strength and tensile strength by 15%, while the ductility increases more than three times as much as compared to that of the base alloy.*
KEYWORDS: *Al-Si-Mg ALLOYS, MAGNETOHYDRODYNAMIC TECHNIQUE, THERMOFORCE TREATMENT, ALLOYING, STRUCTURE*

1. Introduction

The improving the structure and properties of aluminum casting alloys, which are widely used in aviation and rocket technology, is of great interest for today's engineering. The original magnetohydrodynamic (MHD) technique and new smelting technology that relies on magnetohydrodynamic melt mixing are developed by Physico-Technological Institute of Metals and Alloys of the National Academy of Sciences of Ukraine [1, 2]. They can be used to solve the problems of manufacturing high-strength casting aluminum alloys and making castings from them.

Al-Si-Mg alloys are inexpensive alloys with excellent casting properties. They is widely used in the machinery industry, aircraft industry, automotive industry for the manufacture of aircraft suspensions, gearboxes, wheels, tools, bridge members, pump parts and control systems. The widespread use of Al-Si-Mg alloys with high silicon content is due to their good physical, mechanical and technological properties: low coefficient of linear expansion, high modulus, wears resistance and heat resistance [3]. These alloys are good corrosion resistant, perform well at high pressure and high temperature, so they are ideal alloys for high wear applications, as well as engineering alloys with high demands on mechanical properties and tightness. Good casting properties and high tightness of Al-Si-Mg alloys are due to the presence of a large amount of eutectic in them and a narrow crystallization interval. Alloys are strengthened due to the precipitation hardening during the aging as a result of the formation of highly dispersed metastable Mg_2Si hardening phase. But low strength, ductility and machinability – these are disadvantages of those alloys. Although an increase in the Mg content increases the strength of the alloy and improves the machinability, the ductility of the alloy decreases. Improving the properties of Al-Si-Mg casting alloys demands the comprehensive approach both for a choice of melt treatment methods and for determination of heat treatment conditions in solid state to form an optimal structural condition to obtain desired properties.

The combined effect of the new smelting technology that relies on magnetohydrodynamic melt mixing and additional alloying on the structure and properties of the Al-Si-Mg alloy is examined in this paper.

2. Experimental

Hypoeutectic Al-Si-Mg alloy of 356 type was chosen for investigation. The chemical composition of the alloy is shown in Table 1.

Table 1. The chemical composition of the alloy in the initial state.

Alloy	Mg	Si	Mn	Fe	Zn	Zr	Al
A0	0.26	7.0	0.012	0.2	0.01	0.04	base

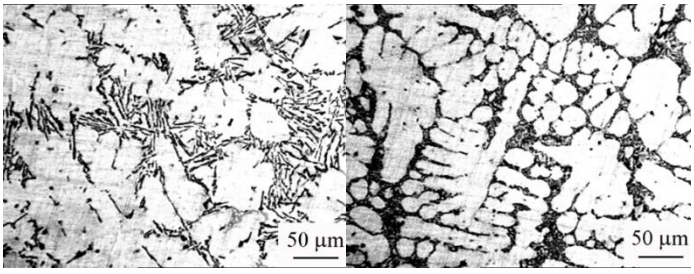
Ingots were melted in the reverberator electric resistance furnace without contact with ferruginous materials. Melt was poured by ladle into the magnetodynamic installation. Metal treatment was carried out in it. Magnetohydrodynamic (MHD) technology enables non-contact, fast-response thermally controlled and force impact on the liquid and solidifying metal. The melt in the working area of MDH-6 installation channel was acted upon by magnetic fields of 0.17 – 0.2 T. The currents were of about 0.17-0.2 kA. In this case vibration with a frequency of 100 Hz was generated in the melt. Pressure in molten metal has caused melt flow in the working area with speed up to 0.2 m/s under conditions of counterflows, vortexes near the working area. The molten alloys were cast into a chill mold, the cooling rate of the ingots was ~ 10 °C/s. Cylindrical specimens of the alloy with the diameter of 20 mm and the length of 200 mm were prepared.

Phase transformations in alloys were studied relying on resistometric method and Vickers hardness measurements. The temperature intervals of the phase transformations were determined by measuring the temperature coefficient of resistivity $\alpha_t=1/\rho_0 \cdot d\rho/dT$ during continuous heating with the rate of 3°C/min in the temperature range of 20 - 500 °C. Mechanical tests were performed using UMM-5 tensile machine on a series of three cylinder-shaped specimens of each studied alloys with the working part of ∅4 mm and l0 = 20 mm at the strain rate $\varepsilon'=2\cdot10^{-3}$ c^{-1}. The structure of alloy in the initial state and after different treatments was examined with NEOPHOT-2 conventional optical microscope.

3. Results and discussion

3.1. Effects of MHD melt treatment on the alloy structure

Metallographic study of the alloy structure was carried out. The microstructure of the alloy in the initial cast state and after MHD treatment is shown in Fig. 1. Metallographic study has shown that the alloy is crystallized with the formation of a dendritic structure. Coarse rod-like eutectic silicon particles are present in the interdendritic space. The macrostructure of the ingot after MHD treatment of the melt, as compared with the initial structure is characterized by the refinement of the grains of the solid solution and structural elements. In this case, as shown by structural studies, the dendritic parameter and the size of rod-like particles decrease. The porosity of the ingot also decreases and the density of the alloy increases.



a b

Fig. 1 The effect of MHD treatment of the melt on the microstructure of Al-Si-Mg alloy: alloy in the initial state (a); after MHD treatment of the melt (b).

The dendritic parameter D, mean sizes d_{max} and d_{min} of Si particles are presented in the Table 2.

Table 2. Structural characteristics of studied alloy.

Treatment of the melt	Dendritic parameter, D, μm	Sizes of Si particles d_{max}/d_{min}, μm
Melting in a resistance furnace	25	40/2
Melt mixing in MHD plant	15	10/1

3.2. Effect of additional alloying on the structure and properties of the Al-Si-Mg alloy

An increase in the mechanical properties of the Al-Si-Mg alloy can be achieved by modifying its structure, as well as by introducing alloying additives. The following factors were taken into account during choosing alloying elements to improve the strength properties of the alloy [4–11]. The alloy is strengthened due to the precipitation hardening during the aging as a result of the formation of highly dispersed particles of the metastable Mg_2Si phase, which is coherently, semi-coherently bonded to the matrix. An increase in the content of magnesium in the alloy provides its further hardening. Additional alloying of the Al-Si-Mg alloy with copper significantly complicates their phase composition. The strengthening phase Al_2Cu, in addition to the strengthening phase Mg_2Si, is formed in the structure after heat treatment. At the same time, the copper content in the alloy should not exceed 2.5-3.0%, because a further increase in the copper content does not lead to the increase in the strength of the alloy, while the ductility decreases due to the presence of Al2Cu particles, that have not been dissolved during heat treatment and corrosion properties deteriorate. Simultaneous alloying of the Al-Si-Mg alloy with titanium, boron and zirconium contributes to the more uniform distribution of alloying elements in the grain of the solid solution, obtaining the dispersed structure and, consequently, improving the mechanical properties of the alloy. Sn, In and Cd are fusible elements, which have minor solubility in Al. Addition of these elements can intensify the nucleation and coalescence of the strengthening metastable Al_2Cu -phase during the decomposition of the supersaturated solid solution. Additional alloying of the alloy with zinc is promising in terms of obtaining high corrosion resistance. The modification of the Al-Si-Mg alloys with elements of the 1st group, such as potassium and sodium, makes it possible to increase their mechanical properties. It is therefore of interest to test lithium, an element of the same group of the Periodic Table, as a modifier of the Al-Si eutectic. The chemical compositions of the alloys studied are shown in Table 3.

Table 2. The dendritic parameter d of the studied Al-Mg alloys.

Alloys	Mg	Si	Cu	Sn	Li	Rose's alloy	Ti	Zn	Al
1	0.44	7.2	1.416	0.158	-	-	-	-	base
2	0.47	5.8	2.26	0.19	-	-	-	-	base
3	0.36	6.5	2.42	-	-	0.2	-	-	base
4	0.33	8.2	-	-	0.2	-	0.158	-	base
5	0.38	7.0	-	-	-	-	0.158	0.93	base

Alloys No 1, 2, and 3 are alloyed with copper and tin. Tin, lead and bismuth are part of Rose's alloy in Alloy No 3. Alloys No 4 and 5 are alloyed with lithium, titanium, and zinc. The change in the dendritic structure of cast alloys depending on the content of alloying elements is shown in Fig. 2.

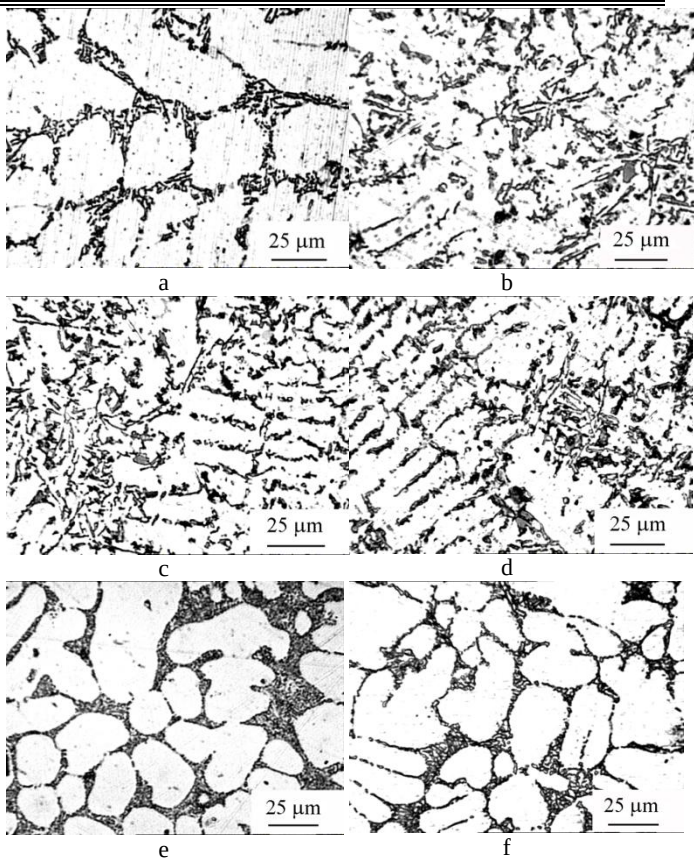


Fig. 2 The effect of alloying on the microstructure of Al-Si-Mg alloy: alloy in the initial state (a), 1 (b), 2 (c), 3 (d), 4 (e), 5 (f).

Signs of a globular structure is observed in the basic experimental aluminum alloy in the initial state after melt treatment, i.e., a globular-dendritic structure is formed (Fig. 2, a). The alloy has a dendritic structure after incorporating copper and tin, precipitates of the equilibrium Al2Cu phase of crystallization origin appear (Fig. 2 b, c, d). The globular-dendritic structure is preserved after alloying the alloy with lithium and titanium (Fig. 2 e) or zinc and titanium (Fig. 2 f). It should be noted that in the base Al-Si-Mg alloy, as well as in alloys No 1, 2, 3 after MHD treatment, Al-Si eutectic particles have an rod-like shape with dimensions dmax/dmin ≈ 10/1 μm. The particles of the Al-Si eutectic in in the alloys No 4 and 5 are equiaxed and much more dispersed than those in the base alloy. The average dimensions of precipitation particles in the alloys No 4 and 5 are ≈ 0.5 μm. It can be seen that lithium is the most efficient Al-Si eutectic modifier.

3.3. Determination of heat treatment modes of the Al-Si-Mg alloys

To eliminate dendritic liquation (microsegregation) that appears during dendritic crystallization, homogenization annealing was used. When choosing the homogenization temperature, it was taken into account that the heat treatment of the Al-Si-Mg alloy is carried out according to the T6 mode [4]. The effectiveness of a two-stage heat treatment scheme according to the T6 mode at low temperatures was tested: annealing 510 ℃ + 535 ℃ to prevent flashing along the grain boundaries. To specify the homogenization regimes, a comparative analysis of changes in the temperature coefficient of resistance $\alpha_T = f(T)$ during continuous heating at a rate of 3 °/min in temperature range from 20 ℃ to 500 ℃. Two modes of alloy homogenization were tested: annealing 510 °C for 2 h + 535 °C for 6 h and annealing 510 °C for 2 h + 535 °C for 10 h followed by water quenching. The obtained curves of changes in the temperature coefficient of electrical resistivity $\alpha_T=f(T)$ for various heat treatment modes are shown in Fig. 3. The temperature coefficient of the electrical resistivity α_T when there are no phase transformations in the alloy is known to be constant. During aging, the formation of phases is accompanied with the depletion of the

solid solution and the appearance of minima on the curve $\alpha_T=f(T)$, which allows us to determine the temperature ranges of the aging of supersaturated solid solutions. The parameters of the peak, the temperature of the minimum Tmin°C, its width ΔT and amplitude $\Delta\alpha_T$ characterize the kinetics of precipitation of the hardening phases Mg_2Si and Al_2Cu during the dynamic aging at the continuous heating. As can be seen in Fig. 3, the changes in temperature coefficient of electrical resistivity during the heating of the alloy are characterized by complex curves that correspond to different temperature ranges of aging associated with the depletion of the matrix with alloying elements. The highest degree of the supersaturation of the solid solution is observed for all the investigated alloys after homogenization according to the regime: annealing 510 °C for 2 h + 535 °C for 6 h followed by quenching in water.

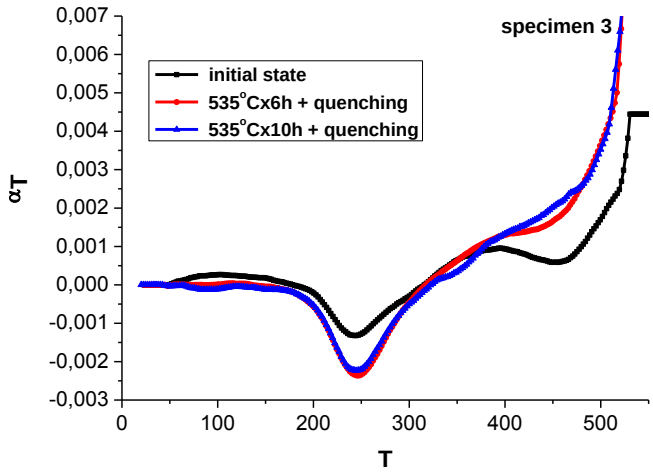


Fig. 3 The change in the temperature coefficient of electrical resistivity $\alpha_T=1/\rho_0 \cdot d\rho/dT$ during continuous heating at the rate of 3 °/min for cast alloy and after quenching and homogenization.

The analysis of the data obtained allowed us the optimal heat treatment mode to be selected: annealing 510 °C for 2 h + 535 °C for 6 h followed by quenching in water and aging at the temperature e of 200 °C for 10 hours.

3.3. Study of the mechanical properties of the alloys

The mechanical properties of the alloys after MHD treatment, homogenization, water quenching and aging at the temperature of 200°C are presented in Table 4.

Table 5. Mechanical properties of the experimental alloys.

Alloys	Yield strength σ_T, MPa	Tensile strength σ_B, MPa	Elongation δ, %	Hv_5 kgs/mm^2
A0	250	294	3,0	83,9
1	320	350	0,8	143,3
2	205	252		153,6
3	345	371	0,6	149,7
4	288	335	9,7	127,8
5	292	333	4,2	128,8

The results of the mechanical tests performed show that the additional alloying of the Al-Si-Mg alloy with Cu and Sn makes it possible to improve the strength characteristics of the alloy due to the precipitation of an additional strengthening phase Al_2Cu during aging. The tensile strength increases by 40% as compared to the base alloy A0,, while the ductility decreases from 3.0 to (0.6-0.8)%. Li proved to be the most effective alloying element that improves the strength characteristics of the alloy. The incorporation of 0.2% Li followed by heat treatment led to a 22% increase in the in the tensile strength, whereas the alloy ductility increases more than three times as much as compared to that of the base alloy A0 due to the modification of the Al-Si eutectic).

4. Conclusion

1. It has been shown that the melt treatment of the aluminum casting alloy based on Al-Si-Mg system in MDH installation allows to obtain a non-dendritic globular structure.

2. The most effective alloying element which improve the strength characteristics of the Al-Si-Mg casting alloy is Li, the introduction of which results in the modification of the Al-Si eutectic and provides an increase in the tensile strength by 22% and ductility - more than 3 times as much as compared to that of the base alloy.

Acknowledgements

This work was carried out within the frame of budget project 055/16 of the G.V. Kurdyumov IMP of the N.A.S. of Ukraine

5. References

[1] Polishchuk V., Tsin M., Gorn R., Dubodelov V. et all, Magnetodynamic Pumps for Liquid Metals, Kiev, Naukova Dumka (1989) (in Russian).

[2] Fixsen W., Ohm L., Trefniak V., Casting Plant and Technology, 2 (2007) 38–39.

[3] Polmear I.J.. Light Alloys: From Traditional Alloys to Nanocrystals, Fourth Edition, Elsevier Butterworth-Heinemann, United Kingdom (2006).

[4] Stroganov G.B., High strength aluminium alloys, Metallurgiya, Moskva (1985) (in Russian).

[5] Hanna M.D., Shu-Zu Lu and A. Hellawell, Modification in the aluminum silicon system. Met. Transact., 15A, № 3 (1984) 459.

[6] Rana R.S., Rajesh Purohit, Das S., Reviews on the Influences of Alloying elements on the Microstructure and Mechanical Properties of Aluminum Alloys and Aluminum Alloy Composites, International Journal of Scientific and Research Publications., 2, Issue 6 (2012) 1. https://www.ijsrp.org/research_paper_jun2012/ijsrp-June-2012-10.pdf.

[7] Stadler F. et al., Effect of main alloying elements on strength of Al–Si foundry alloys at elevated temperatures, International Journal of Cast Metals Research, 25, No 4 (2012) 245. https://doi.org/10.1179/1743133612Y.0000000004.

[8] Pisarek B.P., Rapiejko C., Szymczak T., Pacyniak T., Effect of Alloy Additions on the Structure and Mechanical Properties of the AlSi7Mg0.3 Alloy, Archives of foundry engineering, 17, No 1 (2017) 137.

[9] Nogita K., McDonald S. D., Dahle A. K., Eutectic modification of Al-Si alloys with rare earth metals, Materials Transactions, 45, No 2 (2004) 323.

https://kyushu-u.pure.elsevier.com/en/publications/eutectic-modification-of-al-si-alloys-with-rare-earth-metals.

[10] Voron M.M., Fon Pruss M.A., Byba O. Ye., Microalloying and Modification of Cast Aluminum Alloys for Increasing their Level of Exploitation Properties at Elevated Temperatures. A Review, Casting processes, No 3 (2021) 145. https://doi.org/10.15407/plit2021.03.061.

[11] Bournane M., Berezina A., Davydenko O., Monastyrska T., Molebny O., Spuskanyuk V., Kotko A., Effect of severe plastic deformation on structure and properties of Al-Mg-Si alloy of 6060 type, Materials Science and Metallurgy Engineering, Vol. 1, No 2 (2013) 13-21. http://pubs.sciepub.com/msme/1/2/1/index.html.

Study of fatigue failure for carburized carbon steel

Nardeen Al-Saiymari
Russia, Yekaterinburg
Email: mnardeenn@gmail.com

Abstract: *This study presents the effect of carbonation on 1020 carbonate, low fatigue. The carbonation of the samples was carried out at a temperature of 900 ° C and at a variable time of 5-9 hours. After the process of carbonization, the process was carried out with a temperature of 500 ° C and 30 minutes. The hardness of the sample was tested before the Chemical heat treatment was 206.5 HB and the hardness of the carbonated samples at 900 ° C and at 5 hours was 209.3HB and the hardness of the carbonated samples at 900 ° C and for 6 hours was 209.5 HB. The carbonated sample salad was 900 ° C and 9 hours 211.4 HB. The boxes were heated at (850-900) ºC in an electric furnace for different durations or times. Fatigue was tested for samples before and after carbonation carburizing contributed to the improvement in fatigue strength in different proportions. The degree of improvement depended on the depth (thickness) of the hardened layer and on the microstructure of a carburized steel.*
KEY WORDS: *INDUSTRIAL ENGINEERING, FATIGUE FAILURE, CARBURIZING PROCESS, CARBON STEEL, LOW CARBON STEEL, HEAT TREATMENT, FATIGUE STRENGTH, TEMPERATURE, TEST, STRESS.*

1. Introduction

If a component or structure is subjected to repeated stress cycles, it may fail at stresses well below the tensile strength and often below the yield strength of the material. The processes leading to this failure are termed "fatigue". As technology advanced and more equipment, including cars, airplanes, compressors, pumps, turbines, etc., are subjected to repetitive loads and vibration, fatigue became more and more common. When mechanical components are exposed to dynamic stresses, a variety of traits emerge that are challenging to find in a microstructure [6,8,15].

They should have a high toughness for withstanding the dynamic loads and be hard, wear, and fatigue resistant [5,13]. As a result, extensive research and studies were conducted on these topics. By applying surface treatments like case hardening techniques, which are constituted of carburizing in its three forms (solid, gas, and liquid), they aimed to find out the appropriate solution [10]. These processes are all regarded as the most developed defenses against fatigue. By using such treatments, it is possible to increase steel's fatigue strength while also attaining two qualities at once: a high level of surface hardness and the retention of core toughness [9].

2. Methods

Aim and objectives:

- Improve fatigue resistance of low carbon steel.
-Study the effect of case carburizing on fatigue endurance limits of low carbon steel using finite element programs to simulate fatigue limits of low carbon steel

2.1. Materials

The metal used in the experiment was selected as low carbon steel 1020 shaft that 6m in length and 12mm in diameter. This mineral was chosen for its low carbon ratio because the process of the carburizing is carried out for metals with low carbon ratios. The chemical composition of the samples shown in Table 1.

Table 1. *The chemical composition of low carbon steel specimen.*

Content%	Element
0.28-0.23	Carbon, C
0.30-0.60	Manganese, Mn
0.05(max)	Sulfur, S
0.04(max)	Phosphorous, p
Balance	Iron, Fe

2.2. Samples preparation

(a) Specimens: the fatigue testing specimens have been made according to the standard specifications by turning process for testing them by rotating bending using fatigue testing instrument. It is exposed to cyclic loading such as (gear, rotating shafts, and cutting and drawing dies). Fig.1 shows the dimensions of fatigue specimen according to the standard dimensions.

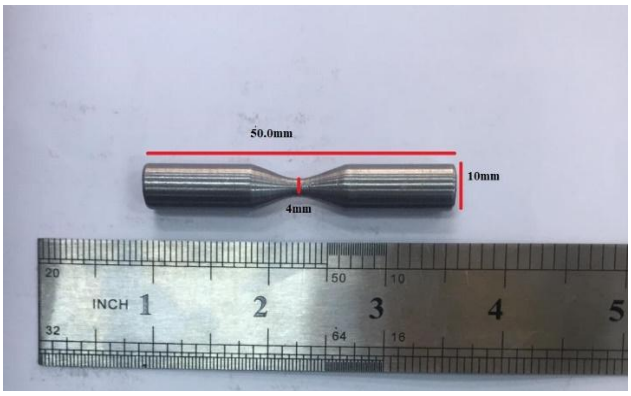


Figure 1. *Fatigue specimen dimensions (all in mm)*

(b) After the samples were cut, the grinding and polishing process was carried out using several grinding wheels ranging from 400 to 1000. For the purpose of obtaining a smooth surface of the sample for a microscopic examination shown in the fig.2. The large ferrite fraction was observed in the microscopic image of the sample compared to the perlite ratio.

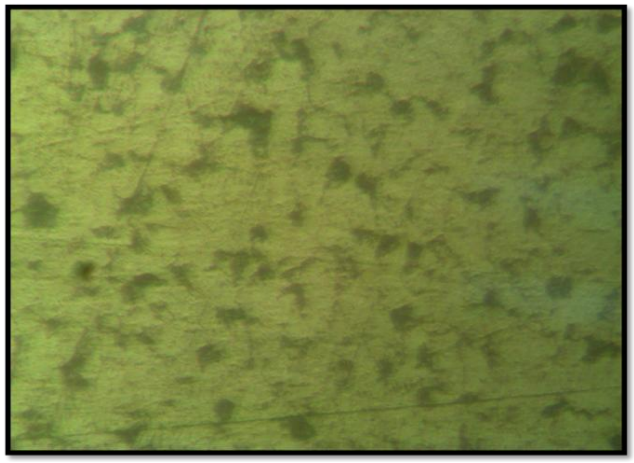


Figure 2. *Micrograph of low carbon steel specimen*

(c) The hardness of the sample was measured to specimens' groups as it is shown in Table 2. by using the apparatus Brinell hardness measuring device.

Table 2. *Classification of specimens with their treatments*

Group symbol	Treatment	Hardness (HB)
A	As received	206.5
B	5hr Pack Carburizing	209.3
C	6hr Pack Carburizing	209.5
D	9hr Pack Carburizing	211.4

2.3. Chemical heat treatment

This study includes one of the chemical heat treatments, carburizing process which was carried out in the low carbon alloy steel specimens then; it was followed by heat treatment which came after carburizing, tempering. Solid (pack) carburizing process was carried out by placing the specimens into heat-resisting steel box (carburizing box) (after cleaning them from attached oil) which was covered with fireclay after it was filled with carburizing compound.

The boxes were heated at (850-900) ºC in an electric furnace for different durations or times as is shown in Table 2.

3. Results

Table 3 shows the results of the fatigue test of low carbon steel samples before and after the carbonation process at a constant temperature of 900C and variable time (5,6 and 9 hours).

Table 3. *Result*

samples	Load (N)	Number of cycles
Non-carbonated samples	48.8	115*10^3
	42.13	235.6*10^3
	37.3	560*10^3
Carbonated samples with 5 hours	67.8	483*10^2
	61.22	312.2*10^2
	56.8	232*10^2
Carbonated samples with 6 hours	47.5	60*10^2
	33.17	51.1*10^2
	27.8	36*10^2
Carbonated samples with 9 hours	20.5	480
	21.2	867
	22	1883

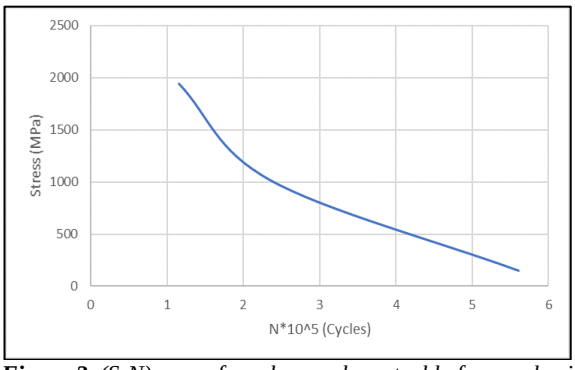


Figure 3. *(S-N) curve for a low carbon steel before carburizing*

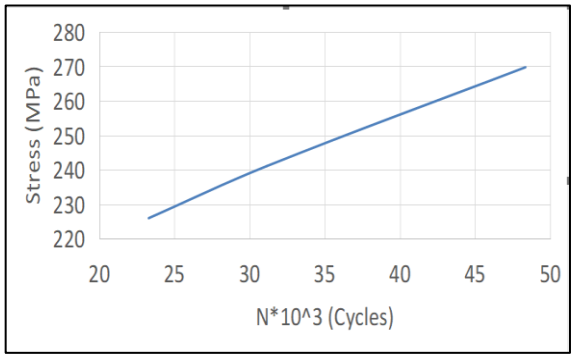


Figure 4. *(S-N) curve for a low carbon alloy steel of solid carburizing at 5 hrs. carburized at 900C.*

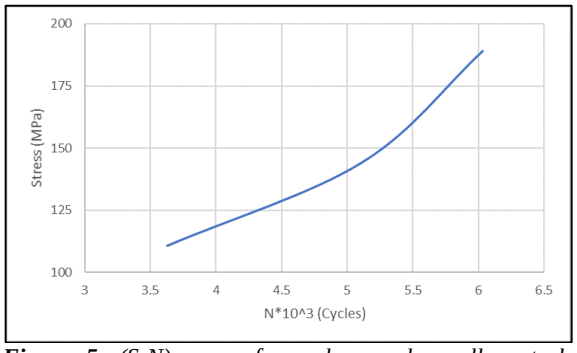


Figure 5. *(S-N) curve for a low carbon alloy steel of solid carburizing at 6 hrs. carburized at 900C.*

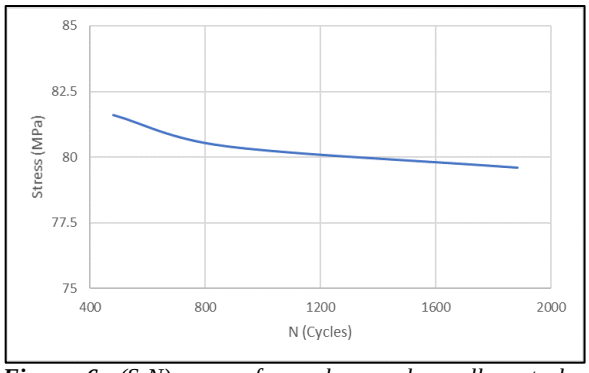


Figure 6. *(S-N) curve for a low carbon alloy steel of solid carburizing at 9 hrs. carburized at 900C.*

3.1. Heat treatment after carburizing

They were tempering was carried out at temperature of 500ºC for 30 minutes then cooled in the furnace to improve core microstructure which was exposed to the overheating during carburizing process [7,11,12].

3.2. Fatigue test

The fatigue test of rotating bending was carried out on rotating fatigue machine. specimen's groups as it is shown in Table 3, with constant amplitude loads stress. Then the (S-N) was obtained for low carbon alloy steel as received (without heat treatment), which was pack.

carburized in duration interval of (5,6, & 9) hr. at temperature of (850-900) ºC in fatigue way which is produced by applying cyclic stresses and finding out fatigue limit (fatigue strength) for each curve.

4. Conclusion

It was found that the depth of hardened layer or case depth will be increased by increasing the time of carburizing at constant temperature 900ºC and then the fatigue strength will be increased as shown in Fig.4. The microstructure of hardened layer or case depth can act as structural barrier and hindering the cracks on the surface and improves fatigue properties of carburized steels [14].

The case hardening of low carbon alloy steel by carburizing results in compressive surface residual stresses and so improves the fatigue strength as shown in Figs.4, 5, and 6.

From the results which had been obtained it was found that the pack carburizing contributes to the improvement of fatigue strength.

The cause is related to the increasing amount of carbon content at the surface, producing compressive stresses and forming structural barrier (martensite), hard phase, a result of phase transformations in steel which participated in hindering the advance of fatigue cracks.

From stress-number of cycles to failure curves (S-N curves) for carburizing, as shown in (Figs.4,5, and 6) respectively it is to be observed that by increasing carburized layer depth (case depth), the fatigue strength and fatigue life will increase which help in increasing the number of cycles necessary to failure. When fatigue strength is compared with solid (pack) carburizing it is found that it and fatigue life is higher than that of carburized layer. This is due to increasing the depth of carburized layer and formation of martensite-dispersed carbide microstructure formed by reheating and quenching carburized steel.

These results confirm that the selection of carburizing method depends on other factors besides the carburizing factors [1]. A few studies [1,2] to evaluate fatigue strength of carburized steel indicate that such treatment is beneficial to the fatigue limit. The selection of carburizing method depends on several factors including the size of the carburized component, geometry, condition of service and operation and economic factor [3,4]. For example, solid carburizing is fit in large parts to give a great carburizing. But for small parts and complex products it would be better to use the gas and liquid carburizing to give it less depth of carburizing.

5. References

[1] Tuck M.A., C. W. “Effect of heat treatment on fatigue strength”, BMPTA Technical Publications, BGA Research, 1999.

[2] Bruce Boardman “Fatigue resistance of steels”, ASM Handbook, Vol 1: Properties and Selection: Irons, Steels, and High-Performance Alloys ASM Handbook Committee, pp. 673688, 1990.

[3] Chta, “datasheet for non-heat-treaters, carburizing and carbonitriding”, Published by the contract heat treatment association, Secratariat, Aston University, UK, 1996.

[4] Osman Asia, Ahmet Çetin Can, James Pineault and Mohammed Belassel “The effect of high temperature gas carburizing on bending fatigue strength of SAE 8620 steel”, Materials and Design ,30,pp. 1792–1797 ,2009 .

[5] Dr.AbdulKhaliq F. Hamood and Dr.Sanna A. hafeed “Influence of annealing, normalizing hardening followed by tempering and laser treatments on some of the static and dynamic mechanical properties of medium carbon steel” , Eng. & Tech. Journal, 28(21),pp. 6274-6287 , 2010.

[6] Craig Friedberg “Fatigue Behavior of Sheet Steels”, M.Sc. Thesis, Mechanical, Industrial & Manufacturing Engineering Department, University of Toledo, 2012.

[7] Liu Shiyong, Liu Deyi and Liu Shicheng “Effect of heat treatment on fatigue resistance of spring steel 60Si2 CrVAT”, Metal Science and Heat Treatment, 52(1-2), pp. 57-60, 2010.

[8] J. Colin, A. Fatemi, and S. Taheri, “Cyclic Hardening and Fatigue Behavior of Stainless Steel 304L”, Journal of Materials Science, Vol. 46, pp. 145-154, 2011.

[9] William D. Callister, Jr. “Materials science and engineering an introduction”, 7th edition, John Wiley & Sons, Inc., 2007.

[10] Mohd Marhan Bin Asari “A study on heat treatment of carburizing carbon steel”, M.Sc. thesis, Faculty of mechanical engineering, university Malaysia Pahang, December ,2010.

[11] Thelning, K-E “Steel and its heat treatment”, 2nd edition, Butterworth, pp. 444 - 482, 1984.

[12] ASM Handbook “Heat treating”, Volume 4, USA, ASM International Handbook Committee, 2001.

[13] Khawla S. Khashan and Oday A. Hamadi “Features of spot-matrix surface hardening of low carbon steel using pulsed laser”, Eng. & Tech. Journal, 25(2), pp. 168-175 ,2007.

[14] Zhang, H.; Shi, Y.; Xu, C.Y.; Kutsuna, M, “Comparison of Contact Fatigue Strength of Carbon Case Hardening and Laser Hardening of Gears”, Surface Engineering, 20(2), pp. 117-120, 2004.

[15] S. McKelvey and A. Fatemi, “Effect of Forging Surface on Fatigue Behavior of Steels: A Literature Review” ,28th Forging Industry Technical Conference, Chicago, IL, April 2011.